Investigating Diurnal and Seasonal Turbulence Variations of the Martian Atmosphere Using a Spectral Approach

Naomi Murdoch, Alexander E. Stott, David Mimoun, Baptiste Pinot, Audrey Chatain, Aymeric Spiga, Orkun Temel, Jorge Pla Garcia, Keisuke Onodera, Ralph Lorenz, et al.

▶ To cite this version:

> Naomi Murdoch, Alexander E. Stott, David Mimoun, Baptiste Pinot, Audrey Chatain, et al.. Investigating Diurnal and Seasonal Turbulence Variations of the Martian Atmosphere Using a Spectral Approach. The Planetary Science Journal, 2023, 4, ⟨10.3847/PSJ/ad06a9⟩. ⟨insu-04472087⟩

HAL Id: insu-04472087

https://insu.hal.science/insu-04472087v1

Submitted on 22 Feb 2024

The Planetary Science Journal, 4:222 (18pp), 2023 November https://doi.org/10.3847/PSJ/ad06a9

Investigating Diurnal and Seasonal Turbulence Variations of the Martian Atmosphere Using a Spectral Approach

Naomi Murdoch[1], Alexander E. Stott[1], David Mimoun[1], Baptiste Pinot[1], Audrey Chatain[2], Aymeric Spiga[3,4], Orkun Temel[5,6], Jorge Pla Garcia[7], Keisuke Onodera[8], Ralph Lorenz[9], Martin Gillier[1], Claire Newman[10], Raphael F. Garcia[1], Lucas Lange[3], and Don Banfield[11]

[1] Institut Supérieur de l'Aéronautique et de l'Espace (ISAE-SUPAERO), Université de Toulouse, Toulouse, France; naomi.murdoch@isae-supaero.fr
[2] Departamento de Física Aplicada, Escuela de Ingeniería de Bilbao, Universidad del País Vasco/Euskal Herriko Unibertsitatea (UPV/EHU), Bilbao, Spain
[3] Laboratoire de Météorologie Dynamique/Institut Pierre Simon Laplace (LMD/IPSL), Sorbonne Université, Centre National de la Recherche Scientifique (CNRS), École Polytechnique, École Normale Supérieure (ENS), Paris, France
[4] Institut Universitaire de France, Paris, France
[5] KU Leuven, Institute of Astronomy, Leuven, Belgium
[6] Royal Observatory of Belgium, Reference Systems and Planetology, Brussels, Belgium
[7] Centro de Astrobiología, (CSIC-INTA), Madrid, Spain
[8] Earthquake Research Institute, The University of Tokyo, Tokyo, Japan
[9] Johns Hopkins Applied Physics Laboratory, 11100 Johns Hopkins Road, Laurel, MD, 20723, USA
[10] Aeolis Research, Chandler, AZ, USA
[11] NASA Ames, Mountain View, CA, USA

Received 2023 May 16; revised 2023 September 29; accepted 2023 October 12; published 2023 November 28

Abstract

We use a spectral approach to analyze the pressure and wind data from the InSight mission and investigate the diurnal and seasonal trends. Our analyses show that the daytime pressure and wind spectra have slopes of approximately −1.7 and −1.3 and, therefore, do not follow the Kolmogorov scaling (as was also previously reported for a reduced data set in Banfield et al.). We find that the nighttime pressure spectral slope is close to −1 (as reported in Temel et al.), and that the wind speed spectral slope is close to −0.5, flatter than the theoretical slope expected for the shear-dominated regime. We observe strong nocturnal (likely shear-generated) turbulent behavior starting around $L_s = 150°$ (InSight sol 440) that shifts to progressively earlier local times before reaching the "5th season" (InSight sols 530–710) identified by Chatain et al.. The diurnal spectral slope analyses indicate an asymmetry in the diurnal behavior of the Martian boundary layer, with a slow growth and fast collapse mechanism. Finally, the low-frequency (5–30 mHz) pressure data exhibit large spectral slope oscillations. These occur particularly during the periods with a highly stable atmosphere and, therefore, may be linked to gravity wave activity.

Unified Astronomy Thesaurus concepts: Atmospheric dynamics (2300); Mars (1007)

1. Introduction

The NASA InSight (INterior exploration using Seismic Investigations, Geodesy, and Heat Transport) mission (Banerdt et al. 2020) landed on Mars in 2018 November in the Elysium Planitia region. The InSight pressure sensor (Banfield et al. 2019) is capable of acquiring data up to 20 Hz; a higher frequency than any previous pressure measurements on the surface of Mars. InSight also has temperature and wind sensors as part of the Temperature and Winds for InSight (TWINS) instrument (Banfield et al. 2019) that acquired data with a sampling frequency up to 1 Hz. The meteorological sensors operated continuously for long periods of time during the InSight mission in order to support the interpretation of the seismological data (e.g., Banerdt et al. 2020; Garcia et al. 2020; Kenda et al. 2020; Lognonné et al. 2020; Charalambous et al. 2021).

Despite not being within the primary goals of the mission and being included as auxiliary measurements (Spiga et al. 2018; Banfield et al. 2019), atmospheric science with InSight has been integral part of the success of the mission (Banfield et al. 2020b). The highly sensitive pressure sensor at the equatorial site of InSight combined with the continuous operation allows the prominent modes of midlatitude planetary waves caused by baroclinic instability to be monitored over seasonal timescales. Measurements of baroclinic waves can be made from orbit (e.g., Hinson & Wilson 2021), but capturing the details at the lowest-scale height is a difficult task and best achieved with continuous measurements on the surface.

InSight also recorded a rich activity of pressure (and, for the strongest events, wind) fluctuations caused by the propagation of gravity waves; for the first time on Mars, bores and long infrasounds—close to the Brunt–Väisälä frequency limit—have been identified in InSight's pressure records. As a turbulence explorer, InSight was a particularly rich experiment. As it is obvious in the very first acquisitions of InSight's pressure sensors, daytime convective vortices are very abundant at InSight's landing site (Banfield et al. 2020b; Lorenz et al. 2021; Spiga et al. 2021); aeolian activity is also strong at InSight in Elysium Planitia, particularly related to vortex activity (Baker et al. 2021; Charalambous et al. 2021) giving rise to tracks visible from orbit (Perrin et al. 2020) although no visible dust devils were imaged by InSight.

The seasonal variability of high-frequency fluctuations of pressure probed by InSight also revealed the high level of turbulence in the dusty season of Mars (Chatain et al. 2021; even featuring nighttime putatively vortex-induced pressure drops) with a subtle combination of increased background wind and reduced stability that gives rise to an active shear-driven convective regime.

The InSight pressure sensor data can also be used to investigate how the planetary boundary layer (PBL) processes vary as a function of frequency, or spectral range. The harmonic analysis of a temporal turbulent field, such as pressure or winds, can help us to understand better the interaction between various meteorological scales, from large coherent eddies to small-scale turbulence. Therefore, the spectral analysis of turbulence is essential to understand the energy cascade of atmospheric turbulence. The static InSight meteorological sensors measure the frequency content of the eddy structures in the atmosphere as they are advected by the ambient wind. Assuming that the turbulent eddies are advected without changes in their properties, and that all eddies are advected with the mean flow velocity (Taylor's frozen turbulence hypothesis; Taylor 1938), single station temporal data can be used to estimate the spatial fluctuations of turbulence. Taylor's frozen turbulence hypothesis also allows analyses to be performed assuming that the wavenumber k has dimensions of inverse time, rather than the usual dimensions of inverse length.

To provide the necessary context for this work, we begin with a brief introduction to the PBL (Section 1.1). We then attempt to summarize the current understanding of using a spectral approach to describe the atmospheric dynamics (Section 1.2) before explaining the objectives of this work (Section 1.3).

1.1. The Planetary Boundary Layer

The PBL (sometimes referred to as the atmospheric boundary layer) is the lowermost part of the atmosphere. This is the part of the atmosphere that is in contact with the planetary surface and is of critical importance for the mixing of heat, momentum, dust, and a variety of chemical species between the surface and atmospheric reservoirs (Petrosyan et al. 2011). Given that all Mars landers have to pass through and operate in the Martian PBL, understanding this part of the Martian environment is also extremely important for the in situ exploration of the red planet.

The atmospheric dynamics of the PBL are strongly influenced by the interactions with the planetary surface, and different types of turbulent regimes exist (Mikkelsen et al. 2017). Specifically, being in close proximity to the surface leads to both thermal instabilities (surface heating produces turbulence via convective instabilities), and mechanical instabilities (due to the vertical shear of the horizontal wind; Petrosyan et al. 2011; Read et al. 2017). The PBL dynamics are also sensitive to changes in the atmosphere's thermal structure.

The Earth's PBL has a different behavior depending on whether the PBL is experiencing near-neutral atmospheric stability conditions (no thermal influence or effects), stable conditions (coldest temperatures close to the ground, typically as a result of nighttime radiation cooling), or unstable conditions (warmest temperatures close to the ground, typically due to solar heating; Mikkelsen et al. 2017). It is the latter, unstable conditions, that tend to enhance the boundary layer turbulence in the daytime (e.g., Senel et al. 2019). An enhanced turbulence implies enhanced atmospheric mixing, more wind gustiness (Stott et al. 2023), and also a larger number of convective cells and vortices, unless the wind shear is particularly strong (Spiga et al. 2021).

As on Earth, the Martian surface temperatures are hotter than the atmosphere during the daytime leading to highly unstable atmospheric conditions. These strong temperature effects lead to discrete ascending thermals, or plumes, and large eddies being generated by buoyancy-driven convection on the scale of the PBL (Petrosyan et al. 2011). With respect to the Earth, Mars has a very low density atmosphere (surface level pressure is only ∼6 mbar) resulting in minimal sensible heat flux between the surface and atmosphere (Spiga 2019). The radiative flux on Mars is, therefore, much larger than the sensible heat flux. However, the majority of the radiative heat passes back up through the thin atmosphere without being absorbed. The consequence is that the sensible heat and radiative heat contributions to the heating of the near-surface (up to ∼1km) atmosphere are typically about equal on Mars (Wu et al. 2021). The daytime convective boundary layer on Mars is typically ∼10 km high (approximately 10 times larger than on Earth; Spiga et al. 2010b). In addition, due to the lower thermal inertia of the Martian surface (Mellon et al. 2000), the day-to-night temperature variations will be higher on Mars. This leads to an even more convective daytime boundary layer, and a shallower nighttime boundary layer on Mars.

At nighttime, however, the atmosphere becomes stable. The turbulence formed by the negative temperature gradient is destroyed by the stable stratification (positive temperature gradient), and the weak turbulence is sustained by the wind shear. Therefore, during the nighttime, wind shear rather than buoyancy dominates the PBL dynamics. This occurs on both Mars and Earth, but nighttime conditions are generally even more stable on Mars than on Earth. The wind shear is largest near the planetary surface (sometimes referred to as the "surface layer," or "eddy-surface layer," e.g., Högström 1990). This is because the wind speed at the ground level is zero resulting in a high level of vertical wind shear (there is a logarithmic height dependence of the wind speed over an aerodynamically rough surface, Prandtl 1935; Bagnold 1941). At larger heights, the shear reduces, reducing in turn the intensity of shear generated turbulence. As a consequence, the nighttime PBL is not only much more stable but also much shallower than the daytime PBL height (on Mars, the nighttime PBL height is hundreds of meters rather than the several kilometers during the daytime). Sometimes, however, turbulent low-level jets can form during the nighttime period both on Earth (e.g., Smedman et al. 1993) and on Mars (Pla-García et al. 2020, 2023).

The structure of the PBL over a diurnal cycle is described graphically in Figure 1. The large and highly unstable daytime PBL (*convective mixed layer*) in which buoyant convection dominates can be seen in addition to the smaller, highly stable, nocturnal boundary layer in which wind shear dominates. The lowest part of the PBL is known as the surface layer.

Several length scales and nondimensional numbers exist to describe the PBL atmospheric dynamics (for a good overview, see Petrosyan et al. 2011). One approach for describing the state of the atmosphere is to compare the rate of buoyant turbulence production (daytime) or destruction (nighttime), B,[12] and the wind shear turbulence generation rate, S[13] (Table 1; and Stull 2017). Under stable conditions, the gradient Richardson number Ri_g can be used to indicate the relative importance of

---

[12] B, the rate of buoyant turbulence production or destruction is defined as $B = |g|/T_v F_H$, where $|g| = 9.8\ \mathrm{m \cdot s^{-2}}$ is the gravitational acceleration magnitude, T_v is the absolute virtual air temperature near the ground, and F_H is the kinematic effective surface heat flux (positive when the ground is warmer than the air). See Stull (2017) for details.

[13] S, the wind shear turbulence generation rate in the surface later, is defined as $S = {u_*}^2 \Delta M/\Delta z$; where ${u_*}^2$ is the friction velocity, M is the wind speed, z is the height above the surface, so $\Delta M/\Delta z$ is the wind shear. See Stull (2017) for details.

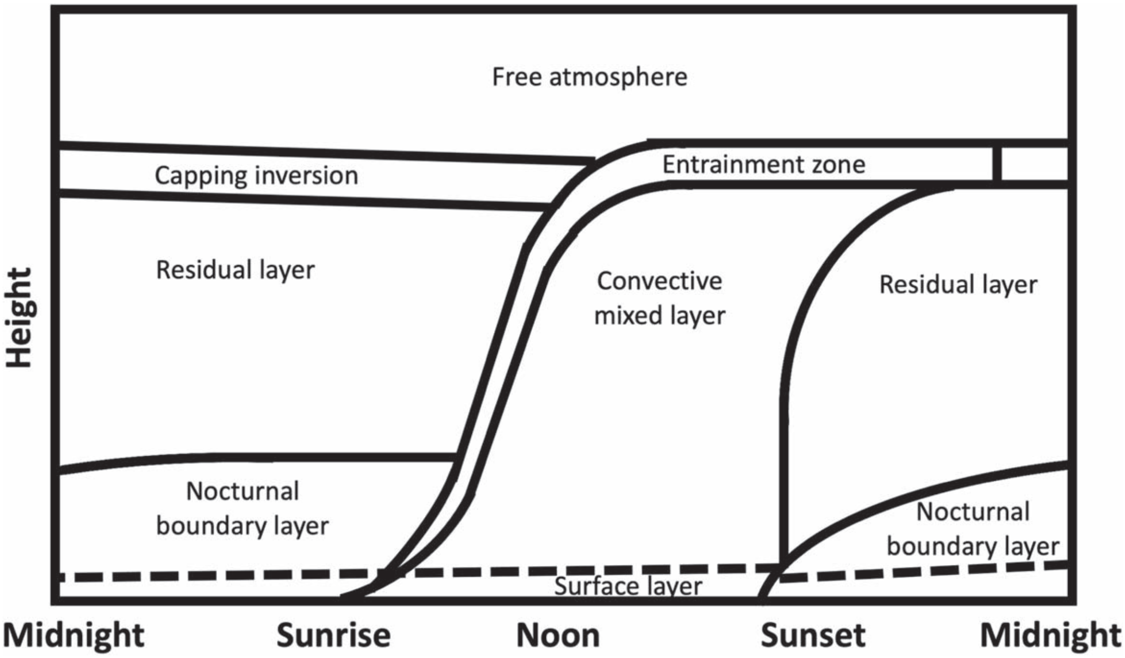

Figure 1. Schematic description of the planetary boundary layer as a function of local time (after Stull 2017). For the Martian atmosphere, the daytime and nighttime boundary layer heights are typically several kilometers and several 100 s of meters, respectively. The terrestrial boundary layer heights are about an order of magnitude smaller than on Mars.

Table 1
Atmospheric States by Relative Rates of Buoyant Turbulence Production, B, and the Wind Shear Turbulence Generation, S, and by the Gradient Richardson Number (after Stull 2017)

Relationship of B and S	Richardson Number Ri_g	Atmospheric State
$B > 0$, $\lvert B\rvert > \lvert 3S\rvert$	$Ri_g < 0$	free (buoyancy-driven) convection (unstable, anisotropic[a] turbulence)
$\lvert B\rvert < \lvert S/3\rvert$	$0 < Ri_g < Ri_c$	forced (shear-driven) convection (stable, isotropic turbulence)
$B < 0$, $\lvert B\rvert < \lvert S\rvert$	$Ri_c > Ri_g > \boldsymbol{Ri_T}$	stably stratified turbulence (weak anisotropic[b] turbulence possible)
$B < 0$, $\lvert B\rvert > \lvert S\rvert$	$Ri_g > \boldsymbol{Ri_T}$	strongly stable, gravity waves possible (no turbulence)
$\lvert B\rvert \sim \lvert S\rvert$	$Ri_g \sim \boldsymbol{Ri_T}$	Kelvin–Helmholtz waves possible

Notes. Ri_g is the gradient Richardson number; Ri_c is the critical value of the gradient Richardson number marking the onset of turbulence whereas Ri_T is the gradient Richardson number marking the termination of turbulence.
[a] More energy in the vertical direction.
[b] More energy in the horizontal direction.

shear production with respect to buoyancy effects: small values of Ri_g indicate that the shear production dominates, and large and negative values of Ri_g indicate an increasing importance of buoyancy effects.

The gradient Richardson number Ri_g is defined as

$$Ri_g = \left(\frac{g}{\theta_0}\frac{\partial\theta}{\partial z}\right)\bigg/\left(\frac{\partial V}{\partial z}\right)^2 \sim -B/S$$

where g is the gravitational acceleration, z is the height above the surface, θ is the potential temperature with $\theta_0 = \theta(z=0)$, and V is the horizontal ambient wind speed. Ri_g is often preferentially used with respect to other nondimensional numbers because the stable boundary layer has well-defined gradients of wind speed and temperature, which are much easier to measure than turbulent fluctuations of wind and temperature (Holden 1998).

There is a critical value of the gradient Richardson number Ri_c, which marks the onset of turbulence. If $Ri_g < Ri_c$, small disturbances superimposed on a laminar flow grow exponentially (i.e., a laminar flow becomes turbulent). A second value of the gradient Richardson number, Ri_T, marks the termination of turbulence (i.e., if $Ri_g > Ri_T$, a turbulent flow becomes laminar; Stull 1988). Ri_c and Ri_T are typically assumed to be 0.25 and 1.0, respectively (Taylor 1931; Miles 1961; Stull 1988). However, it should be noted that the value, and even the existence of Ri_c, is still under discussion in the turbulence literature (e.g., Galperin et al. 2007). Table 1 summarizes the gradient Richardson number for the different atmospheric states.

1.2. A Spectral Description of PBL Turbulence

During daytime, turbulent kinetic energy is typically generated by buoyancy-driven convection (*buoyancy-driven*

Table 2
Theoretical Spectral (Power Spectral Density) Slopes for Different Regimes of Atmospheric Turbulence

Atmospheric Regime	Wind Speed Spectral Slope	Pressure Spectral Slope
Buoyancy-driven production	Variable ($-5/3$ to -3)	Unclear
Shear-driven production	-1	Flatter than $-7/3$
Inertial regime	$-5/3$	$-7/3$
Dissipation regime	-7	Steeper than $-7/3$

Note. See text for explanations and references.

regime) in the form of large eddies at the scale of the PBL. As discussed above, PBL turbulence can also be generated by wind shear and low-level jets, although this is much less prominent than buoyancy-driven turbulence during the daytime. The *shear-driven regime* becomes particularly evident when buoyancy-driven convection reduces (for example, during the stable nighttime atmosphere), or when the energy generated locally by strong wind shear is large. Once generated, the turbulence kinetic energy (TKE) is transferred between large and small scales through nonlinear, inertial interactions (cascading eddies). This is referred to as the *inertial regime*. Eventually, at the very small scale, viscous forces become important, and the eddies are dissipated in the *dissipation regime* (Kolmogorov 1941). Other atmospheric phenomena such as gravity waves and Kelvin–Helmholtz waves may also be present under certain atmospheric conditions (Table 1), but, here, we focus on turbulence rather than waves.

The distribution of turbulent energy over different length-scales is, therefore, described by the PBL turbulent kinetic energy spectrum and may be characterized by a certain power-law slope within each regime. This energy spectrum can be viewed as a superposition of several contributing components (e.g., George et al. 1984; Olesen et al. 1984). The different components will become dominant at different length scales, at different local times and at different heights above the surface. Given that these different components also exhibit different spectral slopes, it is possible to analyze the spectral characteristics as a function of both local time and season in order to probe the Martian atmospheric dynamics. Table 2 provides the theoretical spectral slopes expected for different regimes of atmospheric turbulence. Further details about these regimes and the corresponding theoretical slopes are provided in the following sections.

1.2.1. Buoyancy-driven Turbulence

A buoyancy-driven convection regime (also referred to as free convection) occurs when there are strong temperature effects in the PBL that lead to the generation of large eddies. Bolgiano (1959) suggest from theoretical (physical) arguments that the *horizontal wind speed* spectrum in the buoyancy-driven regime should be proportional to $\sim k^{-11/5}$; however, Weinstock (1978) found that the theoretical spectral slope in the buoyancy regime is not universal. Indeed, it depends on the Richardson's flux number (another Richardson's number that characterizes the thermal stability of the flow defined as the ratio of the buoyant production term and the shear production term) and on the scale size of the energy source and the total kinetic energy (the buoyancy length scale L_b, is given by $L_b = u_h/N$, where u_h is the root mean square of the horizontal wind speed, and N is the Brunt–Väisälä frequency; Weinstock 1978). The typical Brunt–Väisälä frequency in the Martian boundary layer is about about 0.01 Hz (100 s period, estimated at nighttime as poorly constrained at other times; Banfield et al. 2020a); therefore, the buoyancy length scale L_b is typically on the order of a few hundred meters. For length scales shorter than L_b, the effects of buoyancy are not expected to be large enough to change the spectral slope. Then, following Weinstock (1978),[14] for length scales L that are greater than L_b but still relatively short ($L_b < L < 10L_b$), if buoyancy acts as a sink term and destroys turbulence, the power spectral density of the wind speed should have a slope (exponent) larger than $-5/3$ (i.e., $k^{-5/3}$), and the slope can be as large as -2.5. If, however, buoyancy acts as a source of turbulence, the wind speed spectral slope should be smaller than $-5/3$. For length scales that are large with respect to L_b ($L > 10L_b$), they report, interestingly, that the slope can be close to $-5/3$ (the value expected for the inertial regime see below) for the buoyancy regime regardless of whether there is a source or sink of turbulence. Tchen et al. (1985), Avsarkisov (2020) have proposed even steeper theoretical spectral laws ($\sim k^{-3}$) for the wind speed spectral slope in the buoyancy regime ($L > L_b$). It is unclear what the theoretical spectral slope for the *pressure* fluctuations should be in the buoyancy-dominated regime. However, the *pressure* spectrum is related to the density spectrum, and Bolgiano (1959) theoretically derive the density spectrum in the buoyancy regime to be proportional to $\sim k^{-7/5}$.

1.2.2. Shear-driven Turbulence

During the periods of time when there is no, or little, thermal influence in the lower atmosphere, wind shear production dominates. This regime, sometimes referred to as Tchen shear, has been shown to have a theoretical power spectral density for the *horizontal wind speed* of the following form: $F(k) \sim k^{-1}$ (Tchen 1953, 1954; Tchen et al. 1985). The dominant scaling parameter is the shear stress velocity (u_*) sometimes also called the friction velocity (i.e., $F(k) \sim u_*{}^2 k^{-1}$). This scaling has been observed in terrestrial field experiments (e.g., Huang et al. 2021). We were not able to find theoretical spectral slopes for the *pressure* fluctuations in the shear-dominated regime. However, we would expect the shear to flatten the spectral slope resulting in a slope flatter than the theoretical slope of $\sim k^{-7/3}$ in the inertial regime (Section 1.2.3). Temel et al. (2022) report an observed pressure fluctuations slope of -1 for the periods of time in the Martian PBL that are expected to be shear-dominated.

1.2.3. Inertial Regime

In the inertial regime, turbulent eddies (generated through either buoyancy or shear) cascade into eddies of smaller and smaller sizes by an inertial mechanism, and the transfer of energy predominates. George et al. (1984) demonstrate that, as long as the turbulent Reynolds number is sufficiently high, in the inertial regime, the theoretical *wind speed* power spectrum is $F(k) \sim k^{-5/3}$ ($k_0 \ll k \ll \eta^{-1}$), where k_0, is a wavenumber characteristic of the energy-containing wavenumbers. η is the Kolmogorov microscale, which characterizes the dissipative

---

[14] Weinstock (1978) provides these scales in terms of the wavenumber k. Here, we present them in terms of the length scale L using the fact that $L \propto k^{-1}$.

scales and is defined by $\eta = (\nu^3/\epsilon)^{1/4}$, where ν is the kinematic viscosity, and ϵ is the turbulence energy dissipation rate per unit mass. This law is often referred to as Kolmogorov's law (Kolmogorov 1941). The $-5/3$ spectral slope for the *wind speed* power spectrum is also derived by Tchen (1953).

George et al. (1984) also demonstrate that the equivalent theoretical power spectral form for the *pressure* fluctuations in the inertial regime is $\sim k^{-7/3}$. The $-5/3$ and $-7/3$ slopes, for the wind and pressure fluctuations respectively, are often cause for confusion. However, these theoretical expressions are generally well accepted to explain the well-known inertial regime. Several terrestrial studies using observational data have shown that the Earth atmospheric pressure and/or wind speed fluctuations follow the inertial regime scaling at different heights; for example, Nastrom & Gage (1985) use measurements made close to the tropopause and lower stratosphere, and Huang et al. (2021) use measurements from the PBL. The spectral behavior has also been studied in detail in the context of observations of power generation by wind turbines; the turbulent power spectrum follows the inertial regime atmospheric turbulence spectra with frequency f varying as $f^{-5/3}$, or the timescale[15] varying as $\tau^{2/3}$ (Apt 2007; Milan et al. 2013; Bandi 2017).

1.2.4. Dissipation or Viscous Regime

At very small scales, viscous forces become important and the eddies are dissipated. The scale at which the viscous dissipation becomes significant is characterized by the Kolmogorov length scale η defined above (Kolmogorov 1941). Heisenberg predicts that, in this regime, the eddies are not effected by shear and the theoretical *wind speed* power spectrum $F(k) \sim k^{-7}$ (Heisenberg 1948; Tchen 1953). The *pressure* spectrum in the dissipation regime falls off much faster than the inertial $(-7/3)$ power law, as predicted and experimentally observed by Zhao et al. (2016). However, due to the high Reynolds numbers ($R_e > 10^{11}$) on both Earth and Mars (ν is typically $0.001\ \mathrm{m^2\,s^{-1}}$ on Mars Petrosyan et al. 2011), this dissipation regime occurs only at millimetric scales or smaller on Earth and centimetric scales or smaller on Mars (Chen et al. 2016). The measured dissipation rate on Earth (for PBLs formed over flat and homogeneous terrain) is 0.01–0.02 $\mathrm{m^2\,s^{-3}}$ at a height of $\sim$4 m in an unstable surface layer and 0.001–0.005 $\mathrm{m^2\,s^{-3}}$ in the convective mixed layer (Petrosyan et al. 2011). On Mars, the theoretical values calculated using typical Martian PBL parameters are 0.16 $\mathrm{m^2\,s^{-3}}$ in an unstable surface layer and 0.005 $\mathrm{m^2\,s^{-3}}$ in the convective mixed layer (Petrosyan et al. 2011). The associated timescale for the small eddies on Mars, $t_\eta = (\nu/\epsilon)^{0.5}$, is, therefore, $\sim$0.45 s in the convective mixed layer and $\sim$0.08 s in the unstable surface layer. This means that the dissipation regime on Mars should be observable at frequencies above $\sim$2 and $\sim$13 Hz for the convective layer and unstable surface layer, respectively, and perhaps at even higher frequencies depending on the dissipation rate (Temel et al. 2021). As the InSight pressure sensor data only provides reliable data to frequencies up to 2 Hz (Banfield et al. 2020b), in order to sample the dissipation regime on Mars, instruments with much higher sampling frequencies are necessary (for example, the SuperCam microphone on the Mars 2020 Perseverance rover; Maurice et al. 2022; Mimoun et al. 2023).

1.3. Objectives of This Work

The first in situ pressure fluctuations spectrum from the InSight mission was published in Banfield et al. (2020b), where a daytime spectrum averaged over 40 sols (Martian days) was provided. Temel et al. (2022) then elaborated on these analyses by considering how the pressure spectrum varied at a few specific combinations of local times and season. Here, we extend these previous analyses to investigate in detail the Martian diurnal and seasonal spectral dynamics of the pressure measured by InSight. We focus on frequencies $>10^{-3}$ Hz—corresponding to atmospheric variations with a length scale less than the typical depth of a daytime boundary layer on Mars—in order to ensure that we are observing the boundary layer turbulence. At lower frequencies, which will be considered in future publications, we would be looking at larger-scale atmospheric behavior. On these larger scales, the atmosphere behaves more like a two-dimensional incompressible fluid (Fjørtoft 1953; Leith 1971; i.e., meso-scale atmospheric turbulence can dominate over the microscale boundary layer turbulence).

Although such a spectral analysis is only one of many possible methods for probing the flow regime, comparisons between data and the idealized spectral slope values presented in Section 1.2 are important for a simple consideration of the atmospheric dynamics, and also for comparison to models.

In the following, the data and methodology applied are presented in Section 2, and our analysis of both the diurnal and seasonal variations of the pressure and wind spectra are given in Sections 3 and 4, respectively. We finish by summarizing our conclusions and discussing possible interpretations in Section 5.

2. Data and Methodology

In this study, we use the InSight pressure data acquired at 10 samples per second (sps; channel 13.BDO). The first step in the data processing is to identify gaps in the data sets. For data gaps less than 10 samples in duration, we use a nearest neighbor interpolation to fill in the gap. If there are gaps of more than 10 samples, the data set is segmented into separate time series of at least 1 hr. Next, a zero-phase digital filter (<1 mHz) is applied to the data to extract the long period trend. This long period trend is then removed from the pressure data leaving the detrended data with frequencies >1 mHz (see Figure 2). Then, we extract a period of 3600 s from which we calculate the power spectral density (PSD) of the data (pressure or wind speed). Examples for the pressure data from InSight sol 550 (corresponding to 2020 June 13 UTC, solar longitude $L_s = 219°$) at different local times of day can be seen in Figure 3.

As observed for the pressure spectra in Temel et al. (2022), the spectral slope changes as a function of Local True Solar Time (LTST). In some periods of the day, the low and the high frequencies follow the same slope, whereas in others there is a clear slope break indicating a regime change at different frequencies (or length scales). We note also that the wind spectral amplitude is closely linked to the ambient wind speed. This is expected as the area under the spectral curve corresponds to the total energy content of turbulent flow; as

---

[15] As explained in Bandi (2017), τ, the time domain and frequency domain spectral slopes are related as $\tau^{\zeta} = f^{-(\zeta+1)}$.

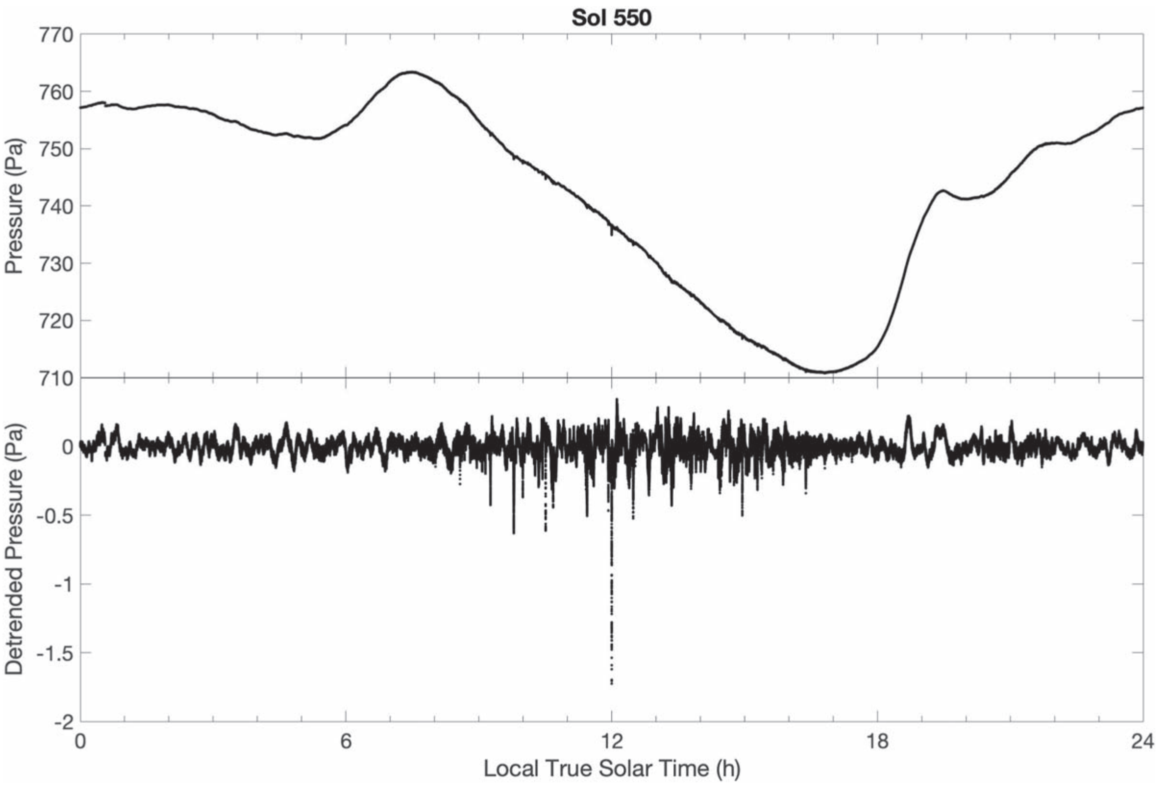

Figure 2. The pressure data (top) and detrended pressure data (bottom) for sol 550 as a function of Local True Solar Time. In the lower data, the long period trend (> 1000 s) has been removed from data.

the wind speed increases, the wind speed fluctuations and thus the TKE also increase. However, here, we focus only on the spectral slope behavior and leave the analyses of the spectral amplitude to other studies.

The InSight meteorological sensors have certain limitations that must be taken into account in the data analysis. The temperature sensor data are very difficult to use for meteorological investigations due to contamination by the lander (Viúdez-Moreiras et al. 2020; Spiga et al. 2021). The wind sensor saturates for wind speeds $\gtrsim 20\,\mathrm{m\,s^{-1}}$, and the characteristic response time of the wind sensor implies that variability above 0.1 Hz in the data cannot be ascribed unambiguously to atmospheric effects; furthermore, when the Reynolds number is low (i.e., for weak winds $\lesssim 2.5\,\mathrm{m\,s^{-1}}$), the wind sensor is not well calibrated and so not capable of providing an accurate wind speed. The pressure sensor provides highly reliable data to frequencies up to 2 Hz; due to mechanical and electronic noise, and a loss of efficiency of the pressure inlet, interpretations of the pressure sensor data should not be made for frequencies above 2 Hz (Banfield et al. 2020b). In this paper, we have decided to focus mostly on the pressure sensor data with frequencies below 1 Hz, but we also discuss the wind data at the end.

Based on these considerations, we determine the best fitting power-law slope (fitted as a linear slope in log-log space) to the data in a low-frequency range (5–30 mHz), and a high-frequency range (0.05–0.5 Hz). Figure 3 shows example PSDs calculated with different levels of smoothing and the associated fits. The low-frequency (5–30 mHz) slope only becomes sensitive to window length when the window used is too small to obtain the required spectral resolution at low frequency. The high-frequency (0.05–0.5 Hz) slope is insensitive to the window length. To avoid problems related to spectral resolution at low frequency, we use the PSD with the largest possible window length to fit the spectral slopes.

Assuming that the length scale is given by the ratio of the horizontal wind speed fluctuations (approximately 0.5–3 $\mathrm{m\,s^{-1}}$, see later Figure 7) to the frequency, this corresponds to length scales of tens of meters to hundreds of meters for the lower-frequency range, and from meters to tens of meters for the higher-frequency range. This process was then repeated every 15 minutes over the course of every sol for an entire Martian year (sols 145–813). This allowed a detailed determination of the typical diurnal variations in spectral slope, and also their seasonal evolution for a full Martian year. The results of these analyses are discussed in the following sections. While this paper focuses on the spectral slopes, Pinot et al. (2023) consider in detail the pressure and wind speed spectral amplitudes, and how they compare with prelanding predictions (Murdoch et al. 2017).

3. Results: Pressure Spectral Slope

3.1. Diurnal Variations of Pressure Spectral Slope

Figure 4 shows the diurnal variation of the mean spectral slope in the two frequency bands over the full Martian year. The diurnal trend can be seen most clearly in the higher-frequency band (0.05–0.5 Hz). During the nighttime (when we would expect to find the shear-dominated regime), the pressure spectral slope is close to -1. The slope then increases in magnitude to an average value of -1.65 ± 0.02 in the daytime period (10–14 LTST), consistent with the initial InSight pressure spectral slope for the unstable convective (daytime) period presented in Banfield et al. (2020b), Temel et al. (2022).

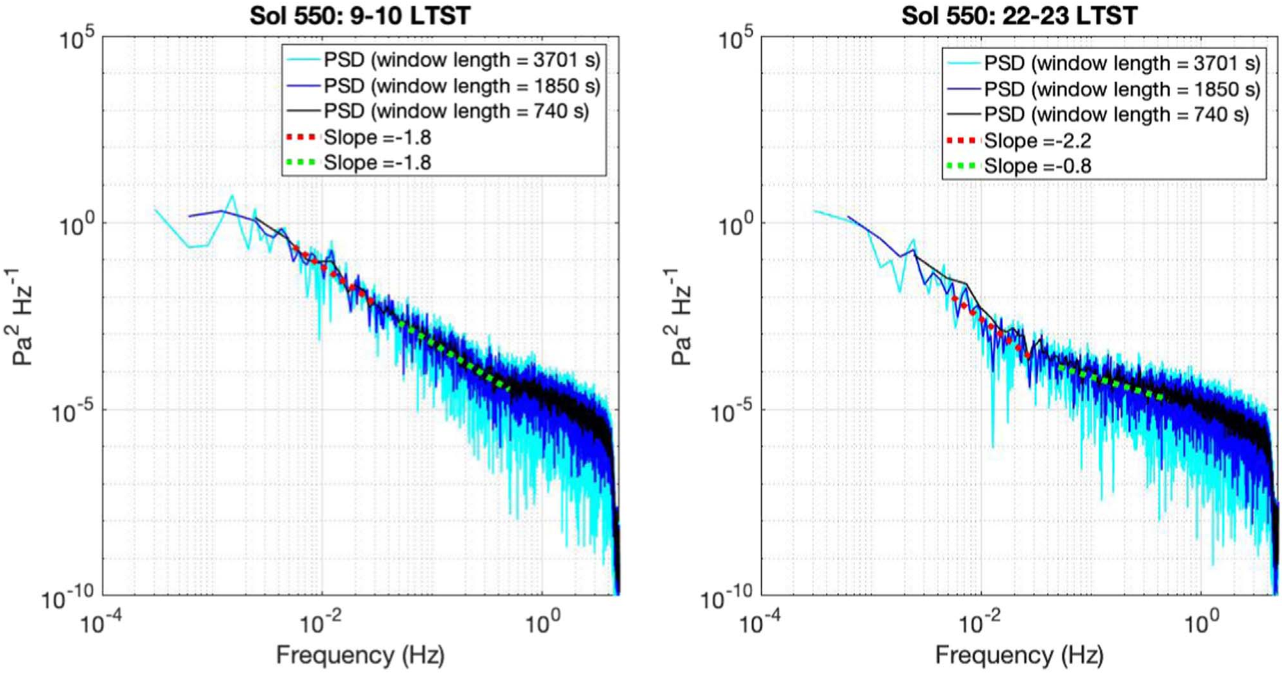

Figure 3. Power spectral densities (PSDs) of the pressure fluctuations on sol 550 in the periods 9–10 Local True Solar Time (left), and 22–23 Local True Solar Time (right). The PSDs are shown with three levels of smoothing dictated by the different window lengths used (cyan = 3701 s, blue = 1850 s, and black = 740 s). The best fitting linear slopes (in log-log space) to the data over the frequency range 5–30 mHz and 0.05–0.5 Hz are shown in the red and green dashed lines, respectively.

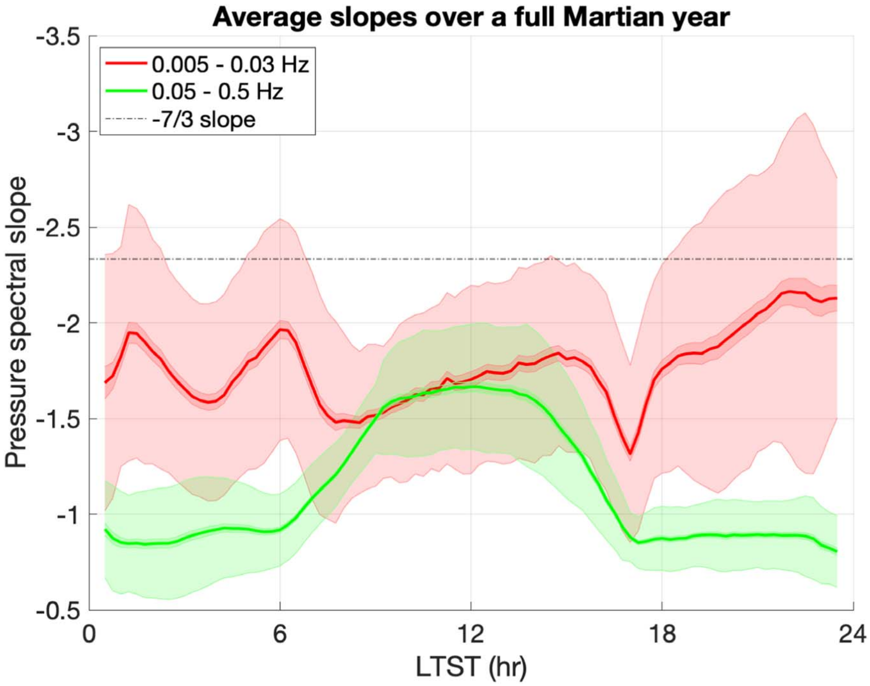

Figure 4. Mean spectral slope of the pressure fluctuations over a full Martian year, as a function of LTST. The slope is the value of the best fitting linear slope (in log-log space) to the data over the frequency range 5–30 mHz (red) and 50–0.5 Hz (green). A bin size of 1 hr (LTST) was used for averaging, calculated every 0.25 hr (LTST). The solid lines represent the mean of the slope measurements within the 1 hr (LTST) bin. The light and dark shaded areas represent the standard deviation (σ) and the 95% confidence intervals of the mean of the slope measurements within the same 1 hr time bin, respectively. The 95% confidence interval is defined as $1.96^*\sigma/\sqrt{N}$, where N is the number of points used to calculate the mean and σ at each local time.

The lower-frequency band (5–30 mHz) includes several interesting features. At the start of the unstable convective daytime period (∼9 LTST), the spectral slope of the lower-frequency band is almost identical to the slope in the higher-frequency band. This indicates that the spectrum is continuous, with no slope break. However, while the 0.05–0.5 Hz slope remains relatively constant over the convective period, the 5–30 mHz slope increases slightly until reaching the steepest slope at the time of the boundary layer collapse (∼16 LTST), at which point there is a sharp and short duration (∼1 hr) flattening of the spectral slope.

This steepening low-frequency daytime slope (changing from −1.5 to −1.8 between the hours of 8 and 15 LTST) is correlated to the increasing height of the PBL throughout the convective period (Read et al. 2017); an increased PBL height implies an increased Richardson number (less shear, more buoyancy) and thus a steeper slope. The steepening spectral slope during the daytime may also be linked to the rate of change of the PBL height, and the associated turbulent length scale, which is proportional to the PBL depth (Temel et al. 2021). The rate of change of the PBL height tends to decrease throughout the day as the PBL tends toward its maximum height (Bianco et al. 2011). The energy spectral transfer rate between different scales can be roughly estimated as v_0^3/l, where v_0 is the turbulent velocity scale, and l is the turbulent length scale (see Equation (5.14) in Davidson et al. 2011). High-resolution atmospheric studies showed that turbulent kinetic energy (the square of turbulent velocity scale) tends to decrease while the PBL reaches its maximum height an hour after local noon until the collapse of the daytime boundary layer (see Figures 1 and 3 in Spiga et al. 2010a). We hypothesize that this decrease in turbulent velocity scales can cause a lower energy spectral transfer rate and may lead to the steepening of the spectral slope. However, it must be noted that, for a complete understanding of the daytime spectral energy transfer, structure functions can be used as in the case of fundamental turbulence studies (Boratav & Pelz 1997; Nie & Tanveer 1999; Toschi et al. 1999), which is beyond the scope of this study.

The boundary layer collapse centered around 17 LTST manifests itself as a smaller absolute value of the spectral slope. This flatter slope may be indicative of a more efficient transfer of energy between large and small scales, i.e., from dissipating large eddies to small-scale nocturnal turbulent structures. The combined observations of the gradually steepening slope in the convective period and the rapid flattening of the slope at the time of the boundary layer collapse are indicative of a slow growth and fast collapse mechanism in the Martian PBL.

We note also that the average slope for the low-frequency band (5–30 mHz) is different during sunrise and sunset. The average slope becomes steeper, tending toward −2 during the growth of the PBL after sunrise (around 6–7 LTST). However, during and after the collapse of the PBL, the slope becomes flatter, tending toward −1.25. This asymmetry implies a difference between the stable-to-convective boundary layer process and the convective-to-stable boundary layer process.

The low-frequency slope varies significantly during the night exhibiting large oscillations, particularly when the atmosphere is very stable (0–6 LTST). In this period, the mean pressure slope oscillates between −1.7 and ∼2. This is discussed in more detail in Section 5.4.

3.2. Seasonal Variations of Pressure Spectral Slope

Figure 5 shows the pressure spectral slope measured as a function of LTST in the two frequency bands over the full Martian year. Spring ($0° < L_s < 90°$) runs from InSight sols 145–306 (and 782–813), summer ($90° < L_s < 180°$) runs from InSight sols 307–485, autumn ($180° < L_s < 270°$) runs from InSight sols 486–627, and winter ($270° < L_s < 360°$) runs from InSight sols 628–781. Figure 6 shows averaged pressure slope values for each of the seasons, and also for the "5th season" with strong nocturnal activity (shear turbulence generated by slope winds) identified by Chatain et al. (2021) from sols 530–710. We use the term "5th season," here, to be consistent with Chatain et al. (2021); however, this period actually covers a large range of L_s and overlaps both the autumn and winter seasons.

Consider the high-frequency (0.05–0.5 Hz) behavior. The behavioral difference between the daytime and nighttime is very obvious in the higher-frequency pressure data (Figure 5, bottom), which show a nighttime spectral slope close to −1 and a convective period slope close to −1.7, as discussed above and previously observed (Banfield et al. 2020b; Temel et al. 2022). There is a very flat (slope ∼−0.5) high-frequency spectral slope in the spring nighttime (see dark blue area at 24-5 LTST from sols 140 to 300; Figure 5, bottom and also Figure 6, bottom). This continues, to a slightly lesser degree, into the summer and decreases with the increased nocturnal activity. Conversely, in season 5, there is an unusually steep high-frequency spectral slope from 0 to 5 LTST (green area in Figure 5, bottom).

Consider, now, the low-frequency (5–30 mHz) behavior. Spring and summer exhibit an increasingly steep spectral slope with LTST during the convective period, whereas the slope value remains stable in autumn and winter (Figure 6, top). As the PBL height is expected to reach larger heights over the course of the day in summer and autumn, this supports our interpretation that the increasing slope corresponds to the increasing height of the PBL. The sharp and short duration (∼1 hr) slope flattening of the lower-frequency slope at the time of the boundary layer collapse (16–17 LTST) is clearly seen throughout all seasons (Figure 5, top and Figure 6, top). The influence of the boundary layer collapse is more extreme in the autumn and winter than in the spring and summer (Fonseca et al. 2018). As discussed in Section 3.1, the much flatter spectral slopes during the autumn and winter boundary layer collapse (∼−1) might be the indicator of a more efficient energy transfer mechanism in these seasons compared with other times of the year. There are also periods of time during the night (often around 20–24 LTST, but also in the period 0–6 LTST during autumn and winter) with very steep spectral slopes (−3; in bright yellow on the top panel of Figure 5), possibly corresponding to gravity wave activity (see discussion in Section 5.4). When considering the mean low-frequency pressure slope as a function of LTST and season (Figure 5, top), the presence of steep spectral slopes at particular times leads to the same oscillations in the mean low-frequency pressure slope as observed in Figure 4. However, here, it can be seen that the amplitude of the pressure slope variation is largest (slope varying from −1.4 to −2.25) during season 5 (black line in Figure 5, top).

There is an unusually flat (slope ∼−1) low-frequency spectral slope during the season 5 night (17-5 LTST). Looking closely at Figure 5 (top), it would appear that there is actually a flattening of the nighttime spectral slope (indicative of increased shear and more efficient energy transfer between large and small scales) starting from sol 400; just after sol 400, this increased nocturnal shear behavior starts to occur about 5 LTST (seen in blue in Figure 5, top), and the shear shifts to progressively earlier local times in the evening before reaching the 5th season. Additionally, this exceptional season exhibits a flatter spectral slope during the full nighttime period, which might be indicative of a long duration, active nocturnal shear (Chatain et al. 2021).

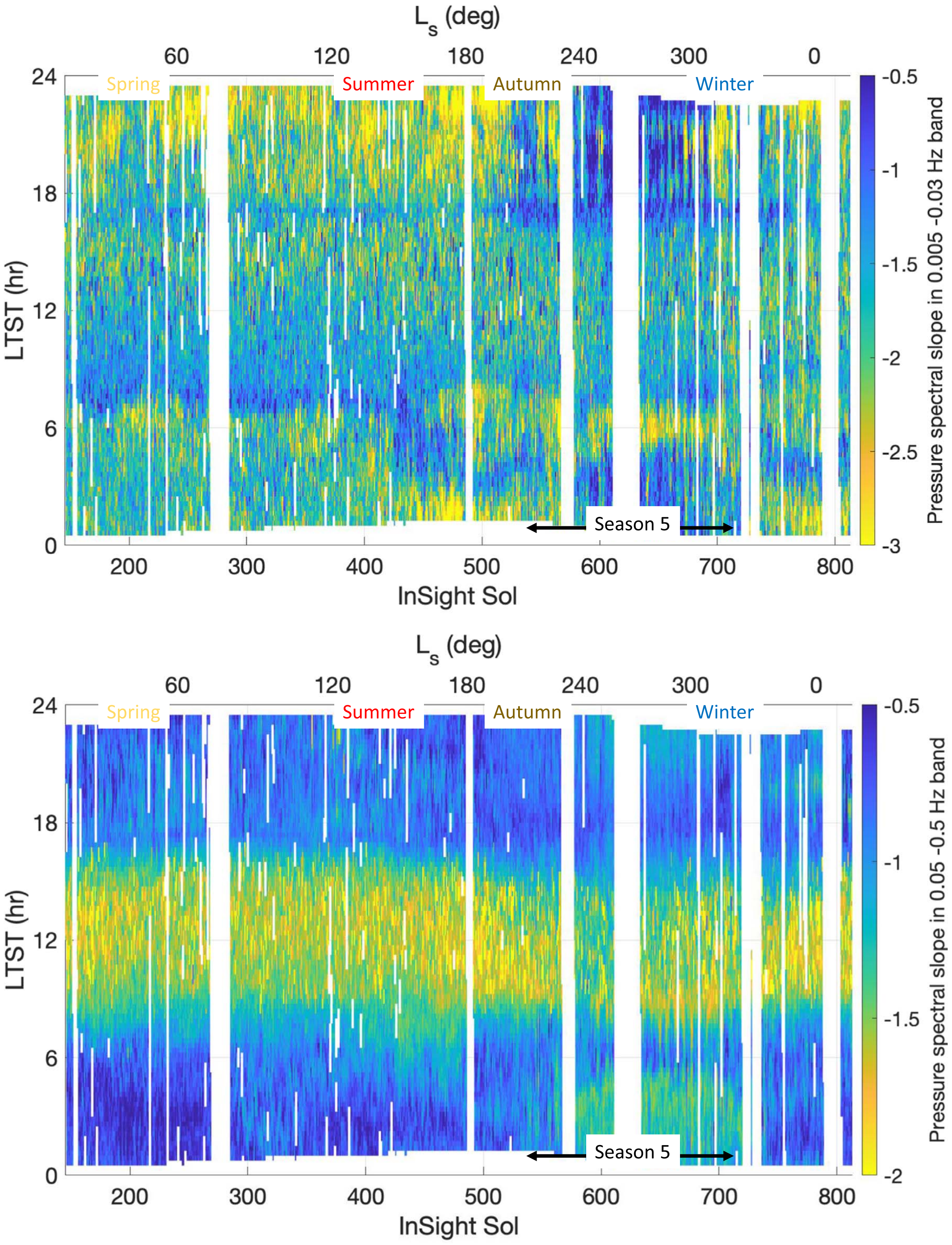

Figure 5. Spectral slope of the pressure fluctuations over a full Martian year, as a function of LTST. The slope is the value of the best fitting linear slope to the data over the frequency range; 5–30 mHz and 0.05–0.5 Hz are shown in the top and lower panels, respectively.

3.3. Relationship between Pressure Spectral Slope and Wind Speed

The ambient wind speed varies significantly as a function of season and LTST (Figure 7, top left) where the ambient wind speed is calculated as the mean of a 1 hr LTST window taken every 0.25 hr. The mean wind speed covaries with the wind speed fluctuations, calculated as the standard deviation of the same 1 hr time window. The joint distribution of the mean and fluctuations of wind speed is shown over the entire sol in Figure 7 (top right), for only the daytime in Figure 7 (bottom left) and only the nighttime in Figure 7 (bottom right). In each case, there is a generally positive correlation between the average and the fluctuations; however, the slope is not always

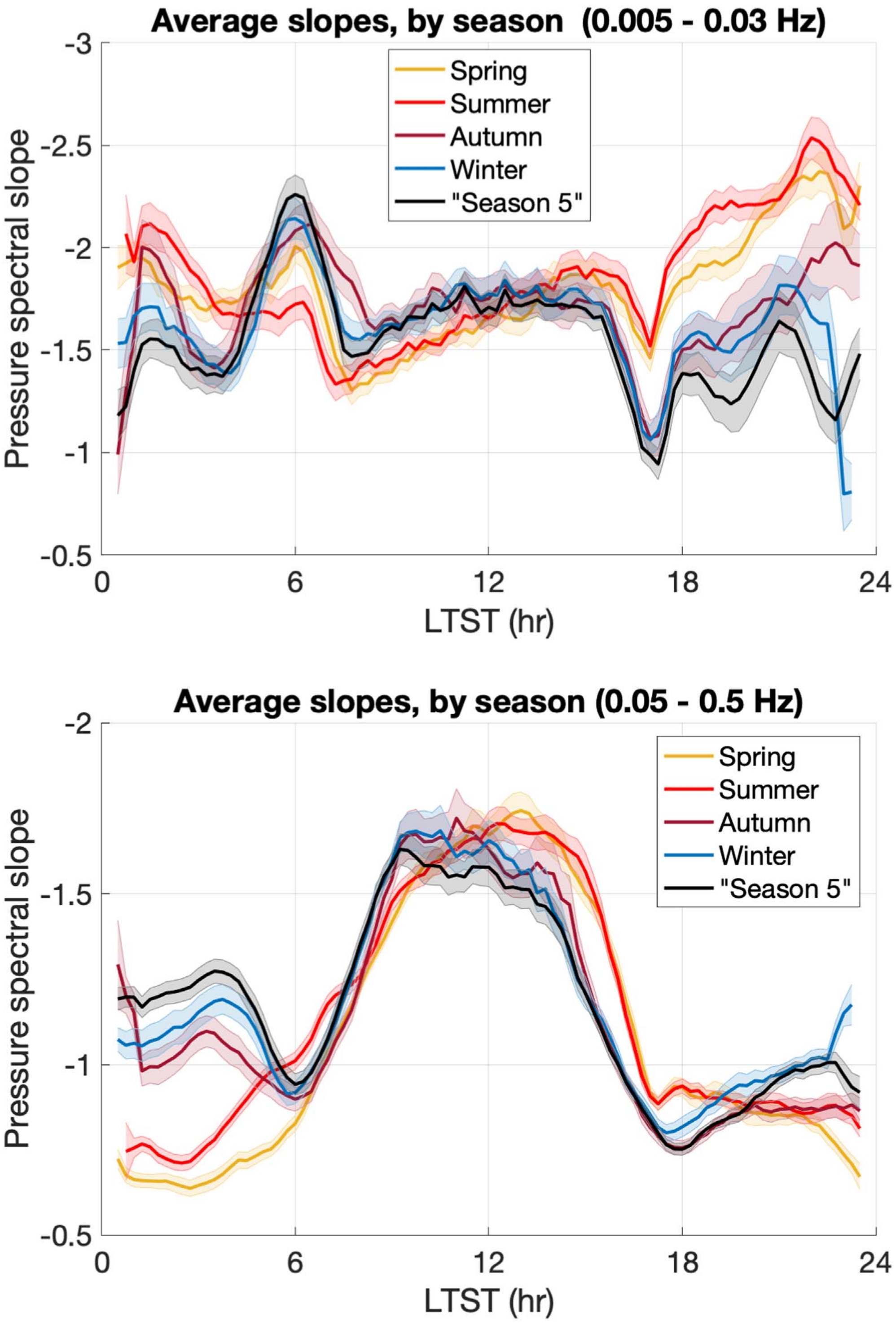

Figure 6. Mean spectral slope of the pressure fluctuations for each season, as a function of LTST, for each frequency bandwidth: 5–30 mHz (top) and 0.05–0.5 Hz (bottom). A bin size of 1 hr (LTST) was used for averaging, calculated every 0.25 hr (LTST). The solid lines and the shaded areas represent the mean and the 95% confidence interval of the mean of the slope measurements within the 1 hr (LTST) bin, respectively, for each season. The 95% confidence interval is defined as $1.96^{*}\sigma/\sqrt{N}$, where N is the number of points used to calculate the mean and standard deviation (σ) at each local time.

the same. Over the full sol, the joint distribution has three main joint distribution peaks: (1) for wind speeds between 2 and 7 $\mathrm{m\,s^{-1}}$ fluctuations between 0 and just over 1 $\mathrm{m\,s^{-1}}$, (2) for wind speeds between 4 and 6 $\mathrm{m\,s^{-1}}$ and fluctuations 2–3 $\mathrm{m\,s^{-1}}$, and (3) for high wind speeds between 8 and 10 $\mathrm{m\,s^{-1}}$ and fluctuations 2–3 $\mathrm{m\,s^{-1}}$. The daytime only joint distributions exhibit the same trimodality with a more pronounced peak in the density at higher wind speeds. On the other hand, the nighttime distribution only consists of the peak associated with lower wind fluctuations. This lower fluctuation region is likely to represent shear-driven turbulence as mechanical instabilities are the main source of turbulence at night. Shear-driven flows may also appear in the hours 6–18 LTST. The higher wind speed region between 8 and 10 $\mathrm{m\,s^{-1}}$ likely represents the main

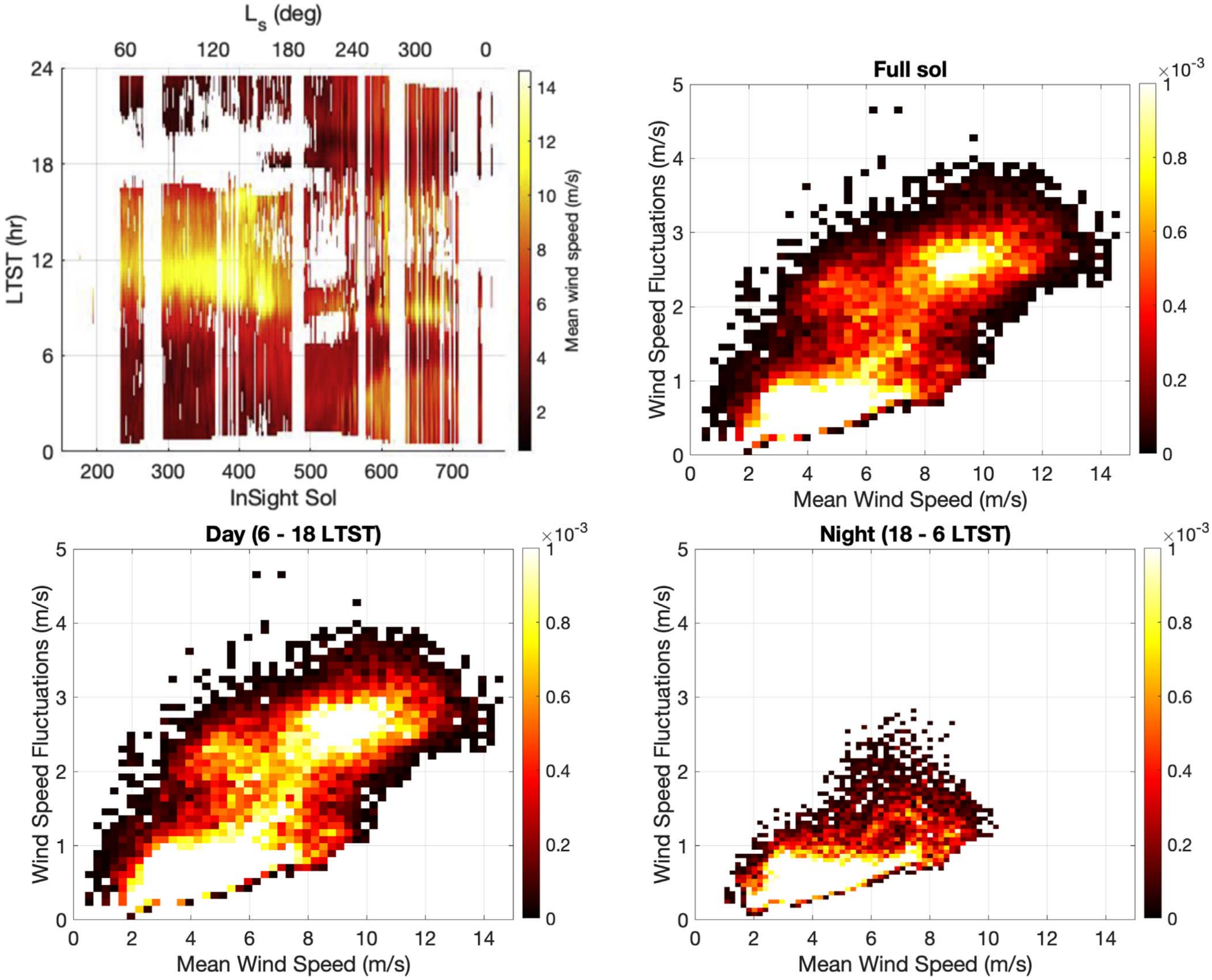

Figure 7. Top left: The horizontal wind speed as a function of local time and sol number as measured by the InSight lander (channel 30.LWS, acquired at 1 sps). The color bar indicates the magnitude of the wind speed. The other three plots show the horizontal wind speed fluctuations as a function of the mean horizontal wind speed as measured by the InSight lander for the full sol (top right), the daytime period (bottom left), and the nighttime period (bottom right). The mean wind speed is the mean of the wind speed data in a 1 hr (LTST) bin, calculated every 0.25 hr (LTST). The wind speed fluctuations refer to the standard deviation of the wind speed data within the same 1 hr (LTST) time period. The color bar represents the probability, i.e., the relative number of observations.

daytime convective period, where the winds are more consistently high along with the fluctuations. The third, less densely populated area (with wind speeds between 4 and 6 m s^{-1} and fluctuations 2–3 m s^{-1}) may represent a transition between the two where the daytime temperature gradient is growing, and winds are gusting more intermittently without yet becoming persistent turbulence, generating large standard deviation but low average wind speeds.

To investigate the relationship of the pressure spectral slope with the ambient wind, we consider how the spectral slope of the pressure fluctuations varies with both the mean wind speed and the amplitude of the wind speed fluctuations (Figure 8). The high-frequency (0.05–0.5 Hz) pressure spectral slope is seen to gradually steepen with increasing wind speed (from -1 to -1.7) indicating the transition from the shear regime (when the buoyancy-driven convection is low and the transfer of energy between large and small scales is very efficient) to the convective regime (when the buoyancy-driven convection increases and the transfer of energy between large and small scales becomes less efficient). The low-frequency (5–30 mHz) spectral slope actually flattens slightly from -2 at low wind speeds to -1.7 when there are stronger background wind speeds. Assuming that a flatter spectral slope implies a more rapid transfer of energy (as discussed in Section 3.1), these observations would imply that the energy transfer between large and small scales is more efficient in the presence of stronger background winds.

When considering the relationship of the pressure spectral slope with the wind speed fluctuations (the standard deviation of the wind speed over the same 1 hr period used to calculate the spectral slope), there are two clear regimes: a low wind speed fluctuation regime (low-frequency slope ~ -2, high-frequency slope ~ -1) and a high wind speed fluctuation regime (slopes of ~ -1.7 in both frequency bands). These two regimes are also visible in the plot of the pressure fluctuations (the standard deviation of the pressure data within a 1 hr LTST time period, calculated every 0.25 hr) against wind speed fluctuations (Figure 9).

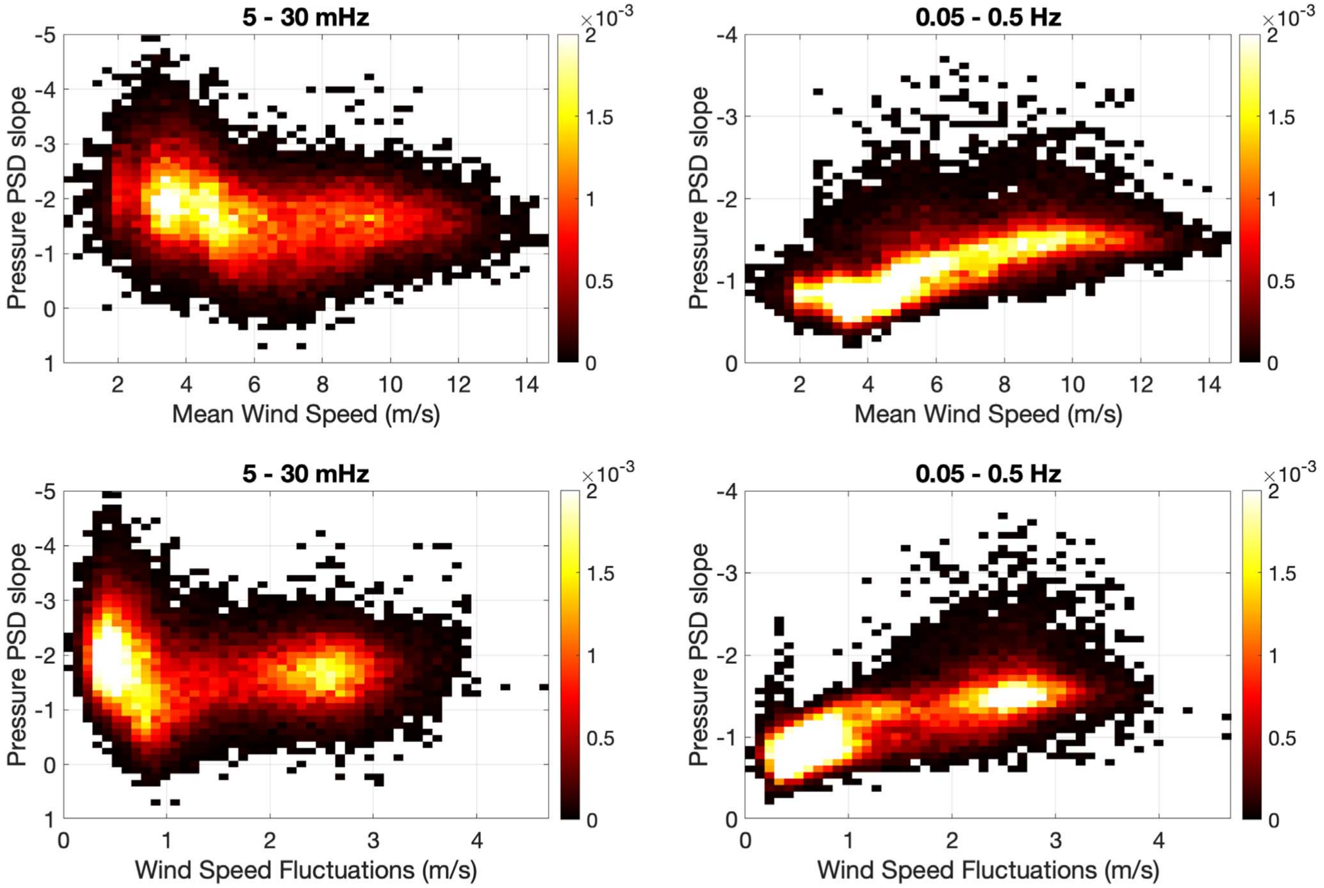

Figure 8. The low- (left) and high- (right) frequency pressure spectral slopes as a function of the wind speed (top) and the wind speed fluctuations (bottom). The mean wind speed is the mean of the wind speed data in a 1 hr (LTST) bin, calculated every 0.25 hr (LTST). The wind speed fluctuations refer to the standard deviation of the wind speed data within the same 1 hr (LTST) time period. The color bar represents the probability, i.e., the relative number of observations.

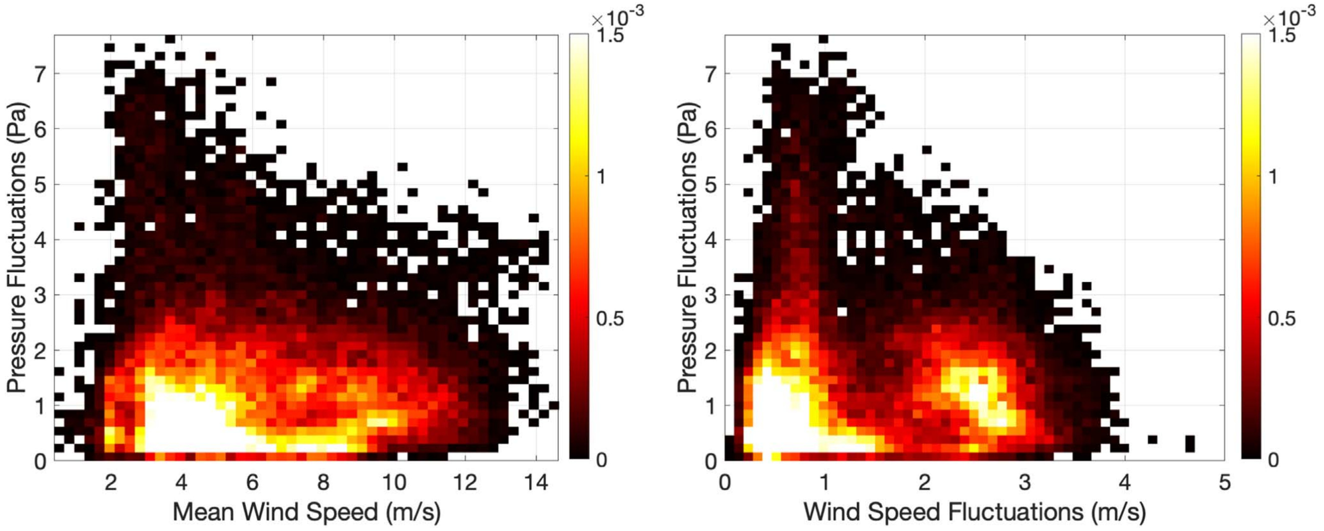

Figure 9. The pressure fluctuations as a function of the mean horizontal wind speed (left) and as a function of the horizontal wind speed fluctuations (right). The mean wind speed is the mean of the wind speed data in a 1 hr (LTST) bin, calculated every 0.25 hr (LTST). The pressure and wind speed fluctuations refer to the standard deviation of the pressure and wind speed data within the same 1 hr (LTST) time period, respectively. The color bar represents the probability, i.e., the relative number of observations.

3.4. The Richardson Number as a Pressure Spectral Slope Predictor

The gradient Richardson number (see Section 1 for details) has recently been used to explain unusually active nighttime behavior observed by InSight in the northern autumn and winter seasons. Chatain et al. (2021) suggest that the weakly positive Ri_g values throughout the night (in the range $0 < Ri_g < 0.25$) lead to conditions that are exceptionally

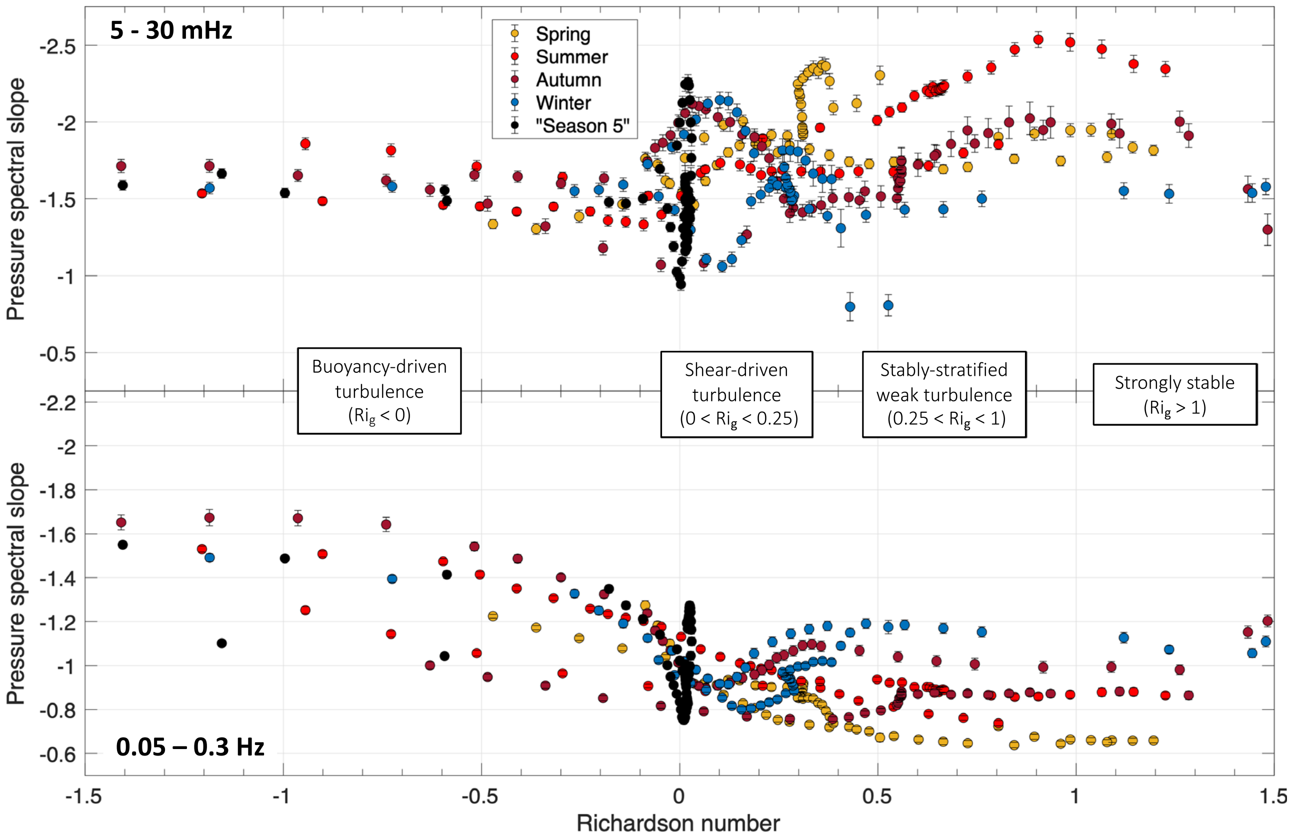

Figure 10. The mean spectral slope of the pressure in the two frequency bands as a function of the gradient Richardson number (as reported in Chatain et al. 2021). The points are color coded by season, and "season 5" refers to the period of strong nighttime turbulence identified in Chatain et al. (2021). The error bars represent the 95% confidence interval on the spectral slope, as defined in Figure 6.

propitious to nighttime shear-driven local turbulence. Here, we use the gradient Richardson number as a function of local time at a height of 6 m above the surface for the different seasons as shown in Chatain et al. (2021). Ri_g is calculated using atmospheric variables from the Mars Climate Database (Millour et al. 2015) for an average year valid for any non-global-dust-storm Martian year like those covered by InSight. This approach was chosen in Chatain et al. (2021) rather than using the InSight air temperature measurements to avoid using temperature data potentially contaminated by lander thermal effects (Banfield et al. 2020b; Spiga et al. 2021).

Figure 10 shows the mean spectral slope of the pressure in the two frequency bands as a function of the gradient Richardson number. The error bars represent the 95% confidence interval on the spectral slope, as defined in Figure 6. We note that season 5 (black markers in Figure 10) has a particularly strong pressure spectral slope variability and is situated at the transition $Ri_g \sim 0$. The spectral slopes for the other seasons appear to exhibit different regimes for different values of Ri_g. There is a clear transition for all seasons around Ri_g=0 (Figure 10). The high-frequency slope is generally flatter when $Ri_g > 0$ compared with when $Ri_g < 0$. On the other hand, the low-frequency slope is steeper when $Ri_g > 0$ compared with when $Ri_g < 0$. In the buoyancy-dominated regime ($\boldsymbol{Ri_g} < 0$), the pressure spectral slopes tend toward −1.7 with decreasing Ri_g in both the high- and low-frequency bands and for all seasons. In the shear-dominated regime ($0 < \boldsymbol{Ri_g} < 0.25$), the pressure spectral slopes are variable but appear to be close to −1.8 at low frequency and −0.9 at high frequency. As the atmosphere becomes more stable ($\boldsymbol{Ri_g} > 0.25$), the high-frequency pressure spectral slope tends to a constant value that depends on the season, the two extremes being −0.65 for spring and close to −1.1 for winter. The low-frequency pressure spectral slope also tends to a constant value with increasing Ri_g that depends on the season, the two extremes being −1.5 for winter and −2.4 for summer. The fact that the steepest low-frequency pressure slopes also occur when the atmosphere, at its most stable, supports the gravity wave interpretation proposed above.

We conclude that the gradient Richardson number appears to be a relatively good predictor of the pressure spectral slope, particularly in the high-frequency bandwidth.

4. Results: Wind Speed Spectral Slope

We have also considered the wind speed data. We use the data acquired at 1 sps (channel 30.LWS) and apply the same processing as for the pressure data (see Section 2; Figure 11). However, due to the wind sensor limitations described above, we only consider the lower-frequency range (5 mHz–0.03 Hz; Figure 12). Figure 13 shows the average wind speed spectral slope measured as a function of LTST in this frequency band over the full Martian year and for each of the seasons, including the 5th season with strong nocturnal activity (Chatain et al. 2021) from sols 530–710.

The wind data are more scarce than for the pressure data, but the diurnal and seasonal trends remain evident. The average wind speed spectral slope is -1.34 ± 0.03 during the unstable convective period (10.5–15.5 LTST), flatter than the theoretically predicted slope value of $-5/3$ for the inertial regime. In

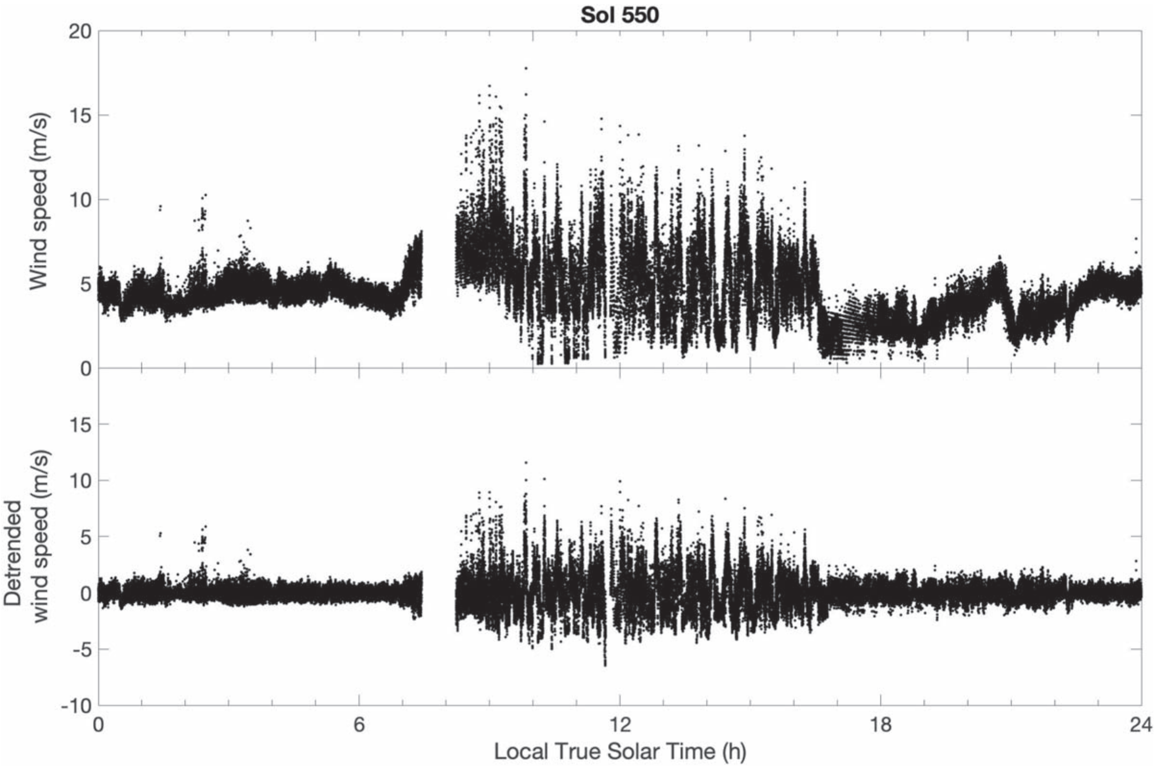

Figure 11. The wind speed data (top) and detrended wind speed data (bottom) for sol 550 as a function of Local True Solar Time. In the lower data, the long period trend (>1000 s) has been removed from data. Periods of time with large data gaps (>10 samples) have been entirely removed from the data set before processing.

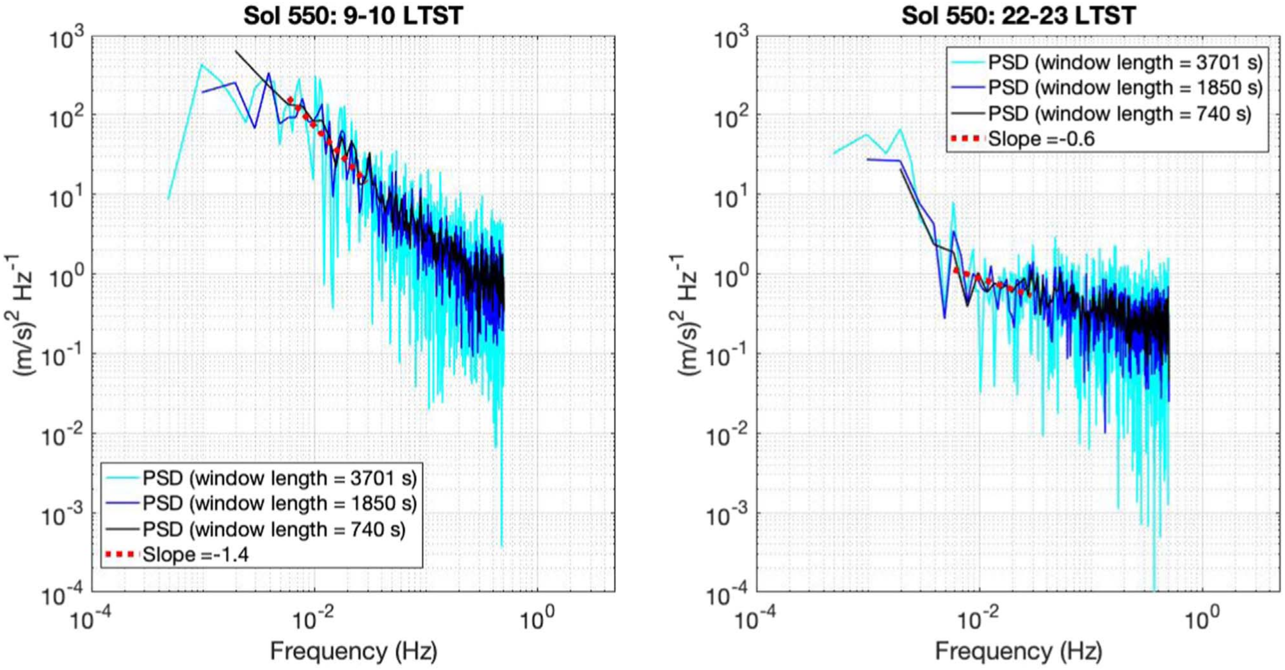

Figure 12. Power spectral densities (PSDs) of the wind speed fluctuations on sol 550 in the periods 9–10 Local True Solar Time (left), and 22–23 Local True Solar Time (right). The PSDs are shown with three levels of smoothing dictated by the different window lengths used (cyan = 3701 s, blue = 1850 s, and black = 740 s). The best fitting linear slope (in log-log space) to the data over the frequency range 5–30 mHz is shown by the red dashed lines.

the spring and summer, the wind speed spectral slope gradually increases during the convective period, reaching a maximum around 13 LTST. This is a similar behavior to the higher-frequency pressure spectral slope (Figure 5), and we associate this with the increasing boundary layer height. In contrast, in autumn and winter, the increase in the wind speed spectral slope is much more rapid, reaching a maximum by 10 LTST (Figure 13).

During the stable nighttime period, the spectral slopes are close to ∼-0.5 for most seasons (Figure 13), and not the value of -1 expected for the shear-dominated regime (Section 1.2.2; and Tchen 1953). With respect to the other seasons, spring and summer

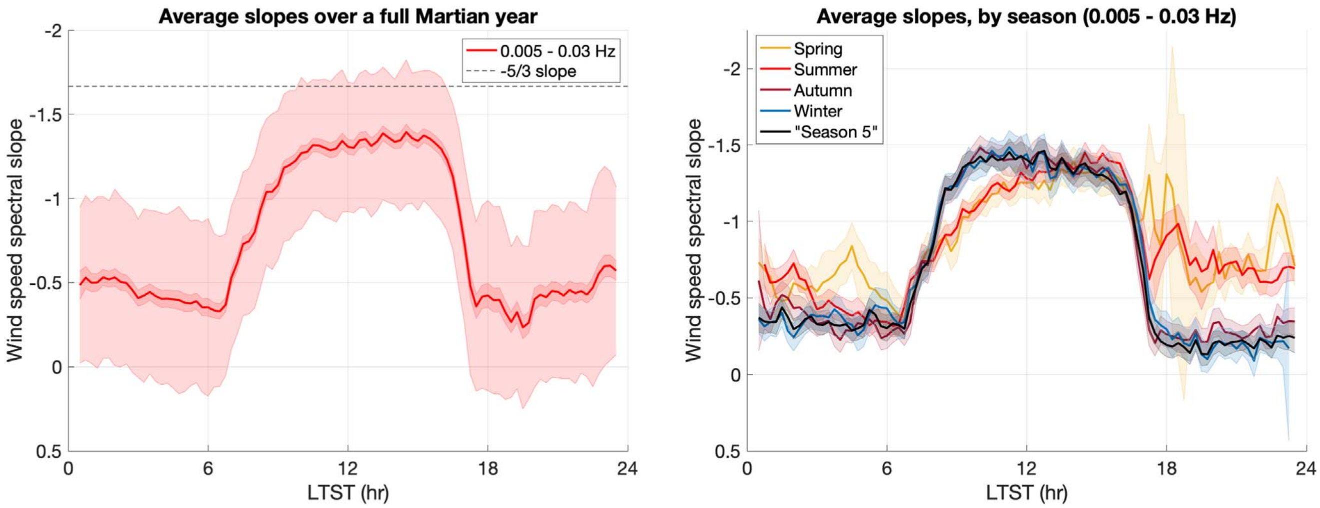

Figure 13. Mean spectral slope of the wind speed fluctuations over a full Martian year (left) and for each season (right), as a function of LTST. The slope is the value of the best fitting linear slope (in log-log space) to the data over the frequency range 5–30 mHz. A bin size of 1 hr (LTST) was used for averaging, calculated every 0.25 hr (LTST). The solid lines represent the mean of the slope measurements within the 1 hr (LTST) bin. In the left figure, the light and dark shaded areas represent the standard deviation (σ) and the 95% confidence intervals of the mean of the slope measurements within the same 1 hr time bin, respectively. In the right figure, the shaded areas represent the 95% confidence interval of the mean slope within the 1 hr (LTST) bin, for each season. The 95% confidence interval is defined as $1.96^{*}\sigma/\sqrt{N}$, where N is the number of points used to calculate the mean and σ at each local time.

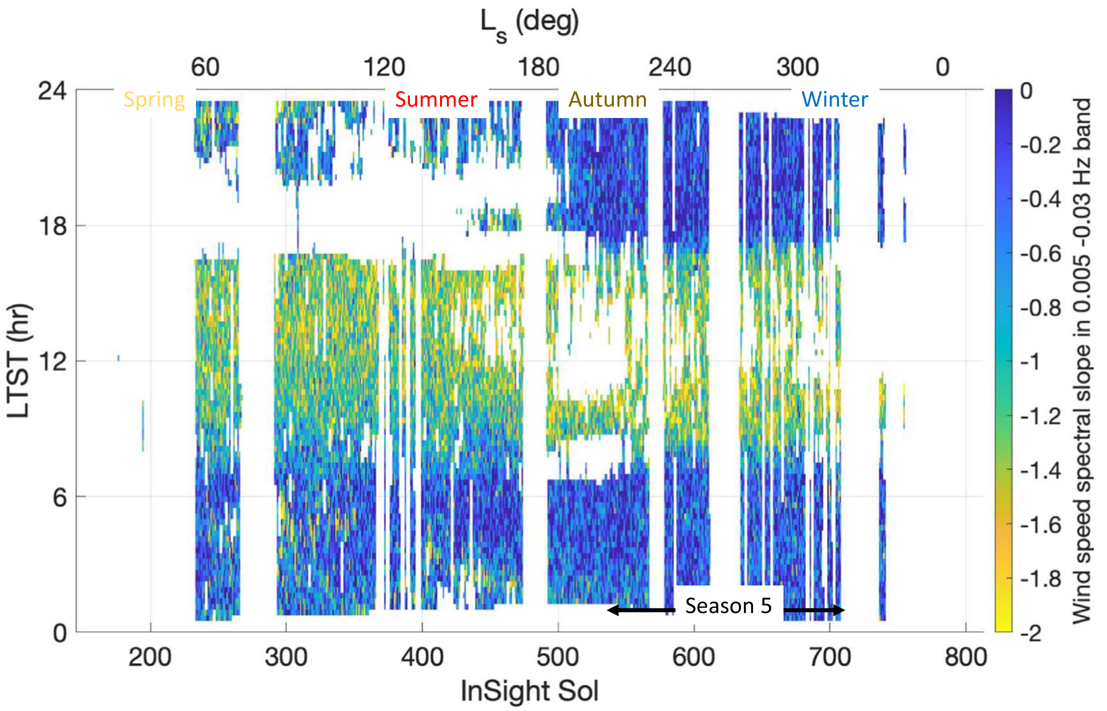

Figure 14. Spectral slope of the wind speed fluctuations over a full Martian year, as a function of LTST. The slope is the value of the best fitting linear slope to the data over the 5–30 mHz frequency range.

periods appear to exhibit a steeper (−0.7 for spring) and significantly more variable spectral slope during the nighttime period (Figure 13, right). However, it should be noted that there are very limited wind sensor data available in the spring and summer in the period 17–20 LTST (see Figure 14). Therefore, we do not attempt to draw conclusions for this time period of spring and summer. Following the boundary layer collapse, autumn and winter periods exhibit very flat (slope close to zero) wind speed spectral slopes (Figure 13, right).

The 5th season (sols 530–710) is less evident in the wind speed spectral slope than in the pressure spectral slope (Figure 14). However, within the same time period as the pressure slope flattening is observed (starting from sol 400 and running to season 5; see Figure 5, top), there is a steeper than average wind speed slope (green and yellow areas from 2-6 LTST, Figure 14).

5. Conclusions and Discussion

We have used a spectral analyses of the InSight pressure and wind data to study the diurnal and seasonal turbulence variations in the Martian PBL. This study is a concrete example as to how Mars' atmosphere could serve as an excellent additional laboratory to Earth's for fluid dynamics studies. Here, we first summarize our key observational results, and, then, below, we discuss some of these results in more detail.

The key results of this paper are as follows:

1. The daytime pressure and wind spectra have average slopes of -1.65 ± 0.02 and -1.34 ± 0.03 and, therefore, do not follow the Kolmogorov scaling ($f^{-7/3}$ and $f^{-5/3}$, respectively), as previously shown for the pressure data (Banfield et al. 2020b; Temel et al. 2022).
2. During the nighttime, the pressure spectral slope is close to -1 (as reported in Temel et al. 2022), and the wind speed spectral slope is ~ -0.5, flatter than the theoretical slope we would expect to find for the wind in the shear-dominated regime (Tchen 1953).
3. The average pressure spectral slope for the low-frequency band (5–30 mHz) is different during sunrise and sunset, indicating an asymmetry in the diurnal behavior of the Martian PBL.
4. The combined observations of the gradually steepening low-frequency pressure spectral slope in the convective period and the rapid flattening of the slope at the time of the boundary layer collapse are indicative a slow Martian convective PBL growth followed by a fast boundary layer collapse.
5. There is an unusually flat (slope ~ -1) low-frequency spectral slope during the full nighttime period of "season 5," which might be indicative of a long duration, active nocturnal shear (Chatain et al. 2021). "season 5" is also preceded by a slope flattening that moves to progressively earlier local times in the evening.
6. Large oscillations can be seen in the low-frequency (5–30 mHz) pressure spectral slope during the nighttime, particularly when the atmosphere is very stable.
7. The joint distribution of wind speed and wind speed fluctuations shows a generally positive correlation with at least three main regions, which may be associated with separate convective, shear-driven, and a transition period with intermittent turbulence.
8. There is a continuum relationship between the pressure spectral slope and the wind speed and fluctuations. This transitions between a low wind speed fluctuation regime (low-frequency slope ~ -2, high-frequency slope ~ -1) present during both daytime and nighttime, and a high wind speed fluctuation regime (slopes of ~ -1.7 in both frequency bands) present only during the daytime. This may represent a transition between shear and buoyancy-driven turbulence.
9. The gradient Richardson number appears to be a relatively good predictor of the pressure spectral slope, particularly in the high-frequency (0.05–0.5 Hz) bandwidth.

5.1. Divergence from Theoretical Kolmogorov Slope Values

Our results show that the daytime pressure and wind spectra do not follow the Kolmogorov scaling ($f^{-7/3}$ and $f^{-5/3}$, respectively), as previously shown for the pressure data (Banfield et al. 2020b; Temel et al. 2022). We suggest that there are three possible reasons for the divergence from theoretical spectral slope values:

1. As InSight is in the surface layer of the Martian PBL, this might suggest that shear contributions to the net pressure spectrum flatten the spectrum at lower frequencies, even during the daytime period. As a consequence, the spectrum of the high-frequency (0.05–0.3 Hz) pressure fluctuations has a slope closer to -1.7 instead of $-7/3$, and the wind spectral slope shows values closer to -1.3 instead of $-5/3$. This superposition of regimes has also been suggested by George et al. (1984), and observed in terrestrial data (the slope of the pressure spectrum was found to be close to $-3/2$ in the surface layer of the terrestrial boundary layer; Albertson et al. 1998). We note that Tillman et al. (1994) also suggested that the inertial regime may be "virtually absent from the turbulence in the Martian atmospheric surface boundary at this height" following analyses of the Viking Landers 1 and 2 wind speed data (measured at a height of 1.6 m above the Martian surface).
2. The underlying hypotheses for our analyses are invalid. Kolmogorov assumes (Kolmogorov 1941) that the turbulent flow is locally isotropic. However, in a shear flow such as in the Martian surface layer, the mean shear rate causes the turbulence to be anisotropic (Pope & Pope 2000). Near to the ground, the horizontal wind speed and standard deviation is often assumed to be more than that of the vertical due to shear effects, for example, in flight gust model specification (Lorenz 2022), breaking the isotropy assumption. Advection and diffusion are also likely to increase anisotropy. In addition, Kolmogorov also requires a high Reynolds number ($R_e \gg 1$) so that the hypothesis of local isotropy is maintained (Kolmogorov 1941). In such a situation, there is a large separation of length scales between the large-scale forcing and small-scale dissipation, and the effect of viscosity is negligible. However, the low surface pressure on Mars leads to slightly lower Reynolds number potentially invalidating the Kolmogorov hypotheses. When investigating the inertial range behavior for varying Reynolds numbers (R_e), Mydlarski & Warhaft (1998) conclude that the inertial range exists but that the velocity spectral slope is a function of R_e, decreasing from $-5/3$ at a high Reynolds number ($R_e \sim 10^4$) to -1.3 at a low Reynolds number ($R_e \sim 10^2$). This conclusion is supported by other observations of a small Reynolds number that do not observe the expected pressure and velocity spectral slopes (Gotoh & Fukayama 2001; Tsuji & Ishihara 2003). Finally, we may also question the assumption of Taylor's frozen turbulence hypothesis for interpreting these in situ data. In particular, it is unsure how well the assumption of frozen turbulence holds across the relevant timescales considered here, and thus how appropriate it is to use a wavenumber with dimensions of inverse time instead of inverse length, as assumed in this work.
3. There are some instrumental effects. Charalambous et al. (2021) demonstrated that the signal power of the InSight pressure data is well correlated to the wind speed. As a result, the pressure sensor data likely contain (or are contaminated by) a dynamic pressure signal, despite the four-disk inlet geometry that is designed to minimize this component.

5.2. An Asymmetrical Martian Boundary Layer with a Slow Growth and Fast Collapse Mechanism

The average pressure spectral slope for the low-frequency band (5–30 mHz) is different during sunrise and sunset indicating an asymmetry in the diurnal behavior of the Martian PBL. This implies a difference between the stable-to-convective BL process and the convective-to-stable BL process. The combined observations of the gradually steepening low-frequency pressure spectral slope in the convective period and the rapid flattening of the slope at the time of the boundary layer collapse are indicative of a slow boundary layer growth followed by a fast boundary layer collapse.

The terrestrial PBLs can have a similar asymmetry in their diurnal variations (Acevedo & Fitzjarrald 2001; Bianco et al. 2011). Such an asymmetry can be caused either by a microscale (local) boundary layer process or by a large-scale (nonlocal) meteorological forcing. On the local scale, factors such as active turbulence (Sorbjan 1997), low-level jets (Smedman et al. 1995) and ageostrophic flow varying with height (Mahrt 1981; Grant 1997; Mahrt 1999) could be playing a role. As for the large-scale (nonlocal) forcing mechanism, clouds can play an important role in terrestrial boundary-layer meteorology (Bianco et al. 2011). Diurnal and seasonal variations in clouds, or generally speaking any volatile or aerosols, can alter the surface radiative balance in planetary atmospheres. On Mars, the dust and water cycles may have a similar impact on the Martian near-surface radiative forcing. From the available data set (surface observations at a single altitude), it is not possible to identify the underlying mechanism with certainty. Nevertheless, we suggest that a local or nonlocal forcing mechanism similar to those observed for Earth's PBL may be happening at the InSight landing site. The fact that this diurnal asymmetry (slow PBL growth and fast collapse) occurs during season 5 winter and autumn but not during spring and summer indicates a seasonality, possibly linked with the interaction between Martian atmospheric cycles and the Martian lowermost atmosphere.

5.3. Evidence for a Transition to Season 5

The 5th season (InSight sols 530–710 as defined in Chatain et al. 2021) with unusually strong nighttime turbulence is clearly visible in the pressure spectral data. We show that around InSight sol 440 the nocturnal shear starts to shift to progressively earlier local times before reaching the 5th season, which exhibits a flatter spectral slope during the full nighttime period indicative of long duration, active nocturnal shear. This transition may be related to the dual Hadley to single Hadley cell transition, or linked to a large-scale wind tendencies shift around $L_s = 180°$ (InSight sol 450, Spiga et al. 2018).

5.4. Large Oscillations in the Low-frequency Pressure Spectral Slope

Large oscillations can be seen in the low-frequency pressure spectral slope during the nighttime, particularly when the atmosphere is very stable, i.e., $Ri_g < 0.25$ (see Figure 4 and the top panels of Figures 5 and 6). This could be interpreted as the presence of waves in the low-frequency pressure (5–30 mHz), rather than the turbulence observed at higher frequencies (0.05–0.3 Hz). These waves may be gravity waves (waves that propagate in a fluid under the influence of gravity), consistent with previous InSight observations (Banfield et al. 2020b; Temel et al. 2022). This interpretation is supported by the fact that the lower bound of the low-frequency range (5 mHz) is slightly below the typical Brunt–Väisälä frequency in the Martian boundary layer (10 mHz). In the presence of gravity waves, the atmospheric density and temperature perturbations cause also oscillations in the wind speed. In previous work looking at the spectrum of Viking Landers 1 and 2, the wind speed data at low frequencies (0.1–50 mHz ; Tillman et al. 1994) observe evidence for gravity waves during times of high atmospheric stability. However, at the frequencies considered here, we do not see evidence for the gravity wave signal in our analyses of the wind data. Seasonal variations may also play a role in the observed larger-scale variations of low-frequency pressure spectral slope (Temel et al. 2022). We speculate that this could occur if gravity waves arise from an interaction of a seasonal jet with Elysium Planitia; the change of general circulation means a change in the source of gravity waves and/or of the gravity wave activity, and thus a marked change in the spectra with season.

Acknowledgments

We thank two anonymous reviewers for their detailed and constructive feedback, which helped to improve the quality of this paper. This study benefited from the financial support of the Centre National d'Études Spatiales (CNES), ISAE-SUPAERO, and the French National Research Agency (ANR) MAGIS project (ANR-19-CE31-0008). A.E.S. is funded by a CNES postdoctoral fellowship. R.L. acknowledges support from the NASA InSight Participating Scientist Program grant 80NSSC18K1626. O.T. is funded by the Research Foundation Flanders (grants 12ZZL20N/12ZZL23N). This is InSight Contribution Number (ICN) 324.

Data Availability

The raw and calibrated APSS data from the InSight mission used in this study are available to the public at the Planetary Data System Geoscience node[16] (Banfield 2019; Rodriguez-Manfredi 2019), at the IPGP Data Center (InSight Mars SEIS Data Service 2019), and at the IRIS Data Management Center[17].

ORCID iDs

Naomi Murdoch https://orcid.org/0000-0002-9701-4075
Alexander E. Stott https://orcid.org/0000-0001-6121-705X
David Mimoun https://orcid.org/0000-0002-3427-2974
Baptiste Pinot https://orcid.org/0000-0003-2180-8650
Audrey Chatain https://orcid.org/0000-0002-2252-3254
Aymeric Spiga https://orcid.org/0000-0002-6776-6268
Orkun Temel https://orcid.org/0000-0002-7222-0948
Jorge Pla Garcia https://orcid.org/0000-0002-8047-3937
Keisuke Onodera https://orcid.org/0000-0003-4120-2437
Ralph Lorenz https://orcid.org/0000-0001-8528-4644
Martin Gillier https://orcid.org/0000-0002-0127-1617
Claire Newman https://orcid.org/0000-0001-9990-8817
Raphael F. Garcia https://orcid.org/0000-0003-1460-6663
Lucas Lange https://orcid.org/0000-0001-6433-1050
Don Banfield https://orcid.org/0000-0003-2664-0164

---

[16] https://pds-geosciences.wustl.edu/missions/insight/index.htm

[17] https://www.fdsn.org/datacenters/detail/IRISDMC/

References

Acevedo, O. C., & Fitzjarrald, D. R. 2001, JAtS, 58, 2650
Albertson, J. D., Katul, G. G., Parlange, M. B., & Eichinger, W. E. 1998, PhFl, 10, 1725
Apt, J. 2007, JPS, 169, 369
Avsarkisov, V. 2020, Atmos, 11, 659
Bagnold, R. A. 1941, The Physics of Blown Sand and Desert Dunes (New York: Methuen),
Baker, M., Newman, C., Charalambous, C., et al. 2021, JGRE, 126, e2020JE006514
Bandi, M. M. 2017, PhRvL, 118, 028301
Banerdt, W. B., Smrekar, S. E., Banfield, D., et al. 2020, NatGe, 13, 183
Banfield, D., Rodriguez-Manfredi, J., Russell, C., et al. 2019, SSRv, 215, 1
Banfield, D., Spiga, A., Forget, F., et al. 2020a, LPSC, 51, 2438
Banfield, D., Spiga, A., Newman, C., et al. 2020b, NatGe, 13, 190
Banfield, D. 2019, APSS PS Data, NASA, Planetary Data System urn:nasa:pds:insight_ps::3.2, NASA, doi:10.17189/1518939
Bianco, L., Djalalova, I., King, C., & Wilczak, J. 2011, BoLMe, 140, 491
Bolgiano, R., Jr 1959, JGR, 64, 2226
Boratav, O. N., & Pelz, R. B. 1997, PhFl, 9, 1400
Charalambous, C., Stott, A. E., Pike, W., et al. 2021, JGRE, 126, e2020JE006538
Chatain, A., Spiga, A., Banfield, D., Forget, F., & Murdoch, N. 2021, GeoRL, 48, e2021GL095453
Chen, W., Lovejoy, S., & Muller, J.-P. 2016, JGRD, 121, 11,968
Davidson, L., et al. 2011, Fluid Mechanics, Turbulent Flow and Turbulence Modeling (Göteborg, Sweden: Chalmers Univ. Tech.)
Fjørtoft, R. 1953, Tell, 5, 225
Fonseca, R. M., Zorzano-Mier, M.-P., & Martín-Torres, J. 2018, Icar, 302, 537
Galperin, B., Sukoriansky, S., & Anderson, P. S. 2007, AtScL, 8, 65
Garcia, R. F., Kenda, B., Kawamura, T., et al. 2020, JGRE, 125, e2019JE006278
George, W. K., Beuther, P. D., & Arndt, R. E. A. 1984, JFM, 148, 155
Gotoh, T., & Fukayama, D. 2001, PhRvL, 86, 3775
Grant, A. 1997, QJRMS, 123, 657
Heisenberg, W. 1948, ZPhy, 124, 628
Hinson, D. P., & Wilson, R. J. 2021, Icar, 357, 114152
Högström, U. 1990, JAtS, 47, 1949
Holden, J. J. 1998, PhD thesis, Univ. Reading
Huang, K., Brunner, C., Fu, M., et al. 2021, ExFl, 62, 76
InSight Mars SEIS Data Service 2019, SEIS raw data, Insight Mission, IPGP, JPL, CNES, ETHZ, ICL, MPS, ISAE-Supaero, LPG, MFSC, doi:10.18715/SEIS.INSIGHT.XB_2016
Kenda, B., Drilleau, M., Garcia, R. F., et al. 2020, JGRE, 125, e2020JE006387
Kolmogorov, A. N. 1941, DoSSR, 30, 301
Leith, C. 1971, JAtS, 28, 145
Lognonné, P., Banerdt, W. B., Pike, W., et al. 2020, NatGe, 13, 213
Lorenz, R. D. 2022, P&SS, 214, 105459
Lorenz, R. D., Spiga, A., Lognonne, P., et al. 2021, Icar, 355, 114119
Mahrt, L. 1981, QJRMS, 107, 329
Mahrt, L. 1999, BoLMe, 90, 375
Maurice, S., Chide, B., Murdoch, N., et al. 2022, Natur, 605, 653
Mellon, M. T., Jakosky, B. M., Kieffer, H. H., & Christensen, P. R. 2000, Icar, 148, 437
Mikkelsen, T., Larsen, S. E., Jørgensen, H. E., Astrup, P., & Larsén, X. G. 2017, PhyS, 92, 124002
Milan, P., Wächter, M., & Peinke, J. 2013, PhRvL, 110, 138701
Miles, J. W. 1961, JFM, 10, 496
Millour, E., Forget, F., Spiga, A., et al. 2015, EPSC, 10, EPSC2015–438
Mimoun, D., Cadu, A., Murdoch, N., et al. 2023, SSRv, 219, 5
Murdoch, N., Mimoun, D., Garcia, R. F., et al. 2017, SSRv, 211, 429
Mydlarski, L., & Warhaft, Z. 1998, JFM, 358, 135
Nastrom, G. D., & Gage, K. S. 1985, JAtS, 42, 950
Nie, Q., & Tanveer, S. 1999, RSPSA, 455, 1615
Olesen, H., Larsen, S. E., & Højstrup, J. 1984, BoLMe, 29, 285
Perrin, C., Rodriguez, S., Jacob, A., et al. 2020, GeoRL, 47, e2020GL087234
Petrosyan, A., Galperin, B., Larsen, S. E., et al. 2011, RvGeo, 49, RG3005
Pinot, B., Mimoun, D., Murdoch, N., et al. 2023, SSRv, submitted
Pla-García, J., Munguira, A., Rafkin, S., et al. 2023, JGRE, 128, e2022JE007607
Pla-García, J., Rafkin, S. C., Martinez, G., et al. 2020, SSRv, 216, 148
Pope, S. B., & Pope, S. B. 2000, Turbulent flows (Cambridge: Cambridge Univ. Press)
Prandtl, L. 1935, in Aerodynamic Theory, Vol. III, ed. W. Durand, III (Berlin: Springer)
Read, P. L., Galperin, B., Larsen, S. E., et al. 2017, in The Atmosphere and Climate of Mars, ed. R. M. Haberle et al. (Cambridge: Cambridge Univ. Press), 172
Rodriguez-Manfredi, J. 2019, APSS TWINS Data, NASA Planetary Data System urn:nasa:pds:insight_twins::3.2, NASA doi:10.17189/1518950
Senel, C. B., Temel, O., Porchetta, S., Muñoz-Esparza, D., & van Beeck, J. 2019, JAMES, 11, 2655
Smedman, A.-S., Bergström, H., & Högström, U. 1995, BoLMe, 76, 211
Smedman, A.-S., Tjernström, M., & Högström, U. 1993, BoLMe, 66, 105
Sorbjan, Z. 1997, BoLMe, 82, 503
Spiga, A. 2019, in Oxford Research Encyclopedia of Planetary Science, ed. R. Peter et al. (Oxford: Oxford Univ. Press), 130
Spiga, A., Banfield, D., Teanby, N. A., et al. 2018, SSRv, 214, 109
Spiga, A., Forget, F., Lewis, S., & Hinson, D. 2010a, QJRMS, 136, 414
Spiga, A., Forget, F., Lewis, S. R., & Hinson, D. P. 2010b, QJRMS, 136, 414
Spiga, A., Murdoch, N., Lorenz, R., et al. 2021, JGRE, 126, e2020JE006511
Stott, A. E., Murdoch, N., Gillier, M., et al. 2023, JGRE, 128, e2022JE007547
Stull, R. B. 1988, An Introduction to Boundary Layer Meteorology, Vol. 13 (Dordrecht: Kluwer)
Stull, R. B. 2017, Practical Meteorology: An Algebra-based Survey of Atmospheric Science (Madison, WI: Sundog Publishing, LLC)
Taylor, G. 1938, RSPSA, 164, 476
Taylor, G. I. 1931, RSPSA, 132, 499
Tchen, C., Larsen, S. E., Pecseli, H., & Mikkelsen, T. 1985, PhyS, 31, 616
Tchen, C. M. 1953, JRNBS, 50, 51
Tchen, C.-M. 1954, PhRv, 93, 4
Temel, O., Senel, C. B., Porchetta, S., et al. 2021, AtmRe, 250, 105381
Temel, O., Senel, C. B., Spiga, A., et al. 2022, GeoRL, 49, e2022GL099388
Tillman, J. E., Landberg, L., & Larsen, S. E. 1994, JAtS, 51, 1709
Toschi, F., Amati, G., Succi, S., Benzi, R., & Piva, R. 1999, PhRvL, 82, 5044
Tsuji, Y., & Ishihara, T. 2003, PhRvE, 68, 026309
Viúdez-Moreiras, D., Newman, C., Forget, F., et al. 2020, JGRE, 125, e2020JE006493
Weinstock, J. 1978, JAtS, 35, 634
Wu, Z., Richardson, M. I., Zhang, X., et al. 2021, JGRE, 126, e2020JE006752
Zhao, S., Cheng, E., Qiu, X., Burnett, I., & Liu, J. C.-c. 2016, ASAJ, 140, 4178